Laboratory study of the collection efficiency of submicron aerosol particles by cloud droplets.
Part II - Influence of electric charges.

Alexis Dépée [1,2], **Pascal Lemaitre**[1*], **Thomas Gelain**[1], **Marie Monier**[2,3], **Andrea Flossmann**[2,3]

[1]   {Institut de Radioprotection et de Sûreté Nucléaire (IRSN), PSN-RES, SCA, Gif-sur-Yvette, 91192, France}

[2]   {Université Clermont Auvergne, Laboratoire de Météorologie Physique, Clermont-Ferrand, France}

[3]   {CNRS, INSU, UMR 6016, LaMP, Aubière, France}

*Correspondence to: Pascal Lemaitre (pascal.lemaitre@irsn.fr)

ABSTRACT

A new In-Cloud Aerosol Scavenging Experiment (In-CASE) has been developed to measure the collection efficiency (CE) of submicron aerosol particles by cloud droplets. Droplets fall at their terminal velocity through a one-meter-high chamber in a laminar flow containing aerosol particles. At the bottom of the In-CASE's chamber, the droplet train is separated from the aerosol particles flow and the droplets are collected in an impaction cup whereas aerosol particles are deposited on a High Efficiency Particulate Air (HEPA) filter. The collected droplets and the filter are then analysed by fluorescence spectrometry since the aerosol particles are atomised from a sodium fluorescein salt solution ($C_{20}H_{10}Na_2O_5$). In-CASE fully controls all the parameters which affect the CE - the droplets and aerosol particles size distributions are monodispersed, the electric charges of droplets and aerosol particles are known and set, while the relative humidity is indirectly controlled via the chamber's temperature. This paper details the In-CASE setup and the dataset of 70 measurements obtained to study the impact of the electric charges on CE. For this purpose, droplets and particles charges are controlled through two charging systems developed in this work - both chargers are detailed below. The droplet charge varies from -3.0x10^4 ± 1.4x10^3 to +9.6x10^4 ± 4.3x10^3 elementary charges while the particle charge ranges from zero to -90 ± 9 elementary charges depending on the particle radius. A droplet radius of 48.5 ± 1.1 μm has been considered for four particle dry radii between 100 and 250 nm while the relative humidity level during experiments is 95.1 ± 0.2 %. The measurements are then compared to theoretical models from literature – showing good agreements.

INTRODUCTION

Aerosol particles (APs) are a fundamental part of the atmosphere since they act on climate and more locally on meteorology (Twomey, 1974). They are also a key topic in human health where APs are known to increase the mortality (Dockery et al., 1992). For these reasons, the processes involved in the removing of the atmospheric AP have been investigated extensively over the last decades, through theoretical works (Slinn and Hales, 1971; Beard, 1974; Slinn, 1974; Young, 1674; Grover and Beard, 1975; Grover et al., 1977; Slinn, 1977; Davenport et al., 1978; Wang et al., 1978; Flossmann, 1998; Santachiara et al., 2012; Tinsley and Zhou, 2015; Cherrier et al., 2017; Dépée et al., 2019) as well as experimental measurements in lab (Kerker and Hampl, 1974; Wang and Pruppacher, 1977; Lai et al., 1978; Barlow and Latham, 1983; Pranesha and Kamra, 1996; Vohl et al., 2007; Ladino et al., 2011; Quérel at al., 2014; Ardon-Dryer et al., 2015; Lemaitre et al., 2017; **Dépée et al., 2020**) and the environment (Volken and Schumann, 1993; Lasko et al., 2003; Chate and Pranesha, 2004; Depuydt, 2013; Laguionie et al., 2014). Far away from the source, APs are mainly scavenged through their collection by clouds and precipitations (Jaenicke, 1993) - referred as the wet deposition. Since it has been reported that the AP collection by clouds prevails in the wet deposition (Flossmann, 1998; Laguionie et al., 2014), the in-cloud AP collection remains an essential issue for the atmospheric sciences.

As previously stated in Part I of this work (**Dépée et al., 2020**) – « In most of current AP wet removal models - like DESCAM (Detailed SCAvenging Model, Flossmann, 1985) - the AP collection is described

50 through a microphysical parameter called "collection efficiency" (CE) which quantifies the ability of
51 a droplet to capture the APs present in its surroundings during its fall. It is the ratio between the AP
52 number (or mass) collected by the droplet over the AP number (or mass) within the volume swept by
53 the droplet for a given AP radius. Another equivalent definition is the ratio of the cross-sectional
54 area inside which the AP trajectories are collected by the droplet over the cross-sectional area of
55 the droplet.
56 Many microphysical effects influence this CE and their contribution is mainly depending on the AP
57 size. To be collected an AP has to deviate from the streamline around the falling droplet to make
58 contact with it. The nanometric AP's trajectory is affected by the collisions with air molecules -
59 referred as the Brownian diffusion. It results in random movement patterns (see Figure 1, A) which
60 tend to increase the CE when the AP radius decreases. For massive APs, there is an increase of CE as
61 they retain an inertia strong enough to deviate significantly from the streamline when it curves and
62 to move straight toward the droplet surface - known as inertial impaction (see Figure 1, B). When
63 considering intermediate AP size, the CE goes through a minimum value called the "Greenfield gap"
64 (Greenfield, 1957) where the AP diffusion and inertia are weaker. In this gap, other microphysical
65 effects can be involved to make the droplet encounter the AP like the interception for instance. It is
66 the collection of APs following a streamline that approaches the droplet within a distance equivalent
67 to the particle radii (a) - see Figure 1, C». Note that there are also thermophoretic and
68 diffusiophoretic forces which can have an influence on the CE. These effects prevail in subsaturated
69 air - as it is the case sometimes in clouds - and are discussed in Part I (**Dépée et al., 2020**).
70 Since droplets are naturally charged in clouds (Takahashi, 1973) as well as the atmospheric APs, there
71 are electrostatic forces which can influence the AP collection. Numerous numerical studies were
72 dedicated to the influence of the electric charges on CE – such as Grover et al. (1975), Jaworek et
73 al. (2002), Tinsley and his group (for instance - Tinsley et al., 2006 or Tinsley and Zhou, 2015). They
74 suggest an increase of the CE of several orders of magnitude even when the AP is weakly charged.
75 However, the AP charge increases when the APs are radioactive (Clement and Harrison, 1992) -
76 inducing an impact on CE even larger (Dépée et al., 2019). Thus, the AP "electroscavenging" in clouds
77 has to be investigated, particularly for nuclear safety issues when the APs removal by clouds result
78 from the discharge of radioactive materials from a nuclear accident. For this purpose, the modelled
79 CEs with electrostatic forces need to be experimentally validated before the incorporation in cloud
80 models. Especially, the analytical expression for electrostatic forces used in numerical studies
81 (Jaworek et al., 2002 ; Tinsley et al., 2006 ; Tinsley and Zhou, 2015 ; Dépée et al., 2019) has to be
82 confirmed by measurements.
83 When a droplet with a charge Q approaches an AP of charge q, the partial influence of the AP
84 electrostatic field on the droplet leads to the re-orientation of the water dipoles. As a result, a
85 surface charge distribution on the droplet is created and supposed to be comparable to the one of a
86 conductive sphere. In an electrostatic equivalent problem, the droplet can be replaced by two-point
87 charges (Jackson, 1999). One modelling the charge distribution, inside the droplet and near its
88 surface, another for the residual droplet charge located at the droplet surface. Finally, the analytical
89 expression of the electrostatic forces is the addition of two Coulomb forces between the AP and the
90 two-point charges inside the droplet. The factored expression can be found in equation (10) and
91 further details can be found in Tinsley et al. (2000). It consists of two terms. The first one is the
92 Coulomb inverse square term which prevails in the AP collection for large enough AP electrical
93 mobilities or electric charge products ($q \times Q$), attractive (Figure 1, D) or repulsive (Figure 1, E)
94 depending on whether the AP charge (q) and the droplet charge (Q) have unlike or like signs. The
95 second term is referred as the short-range attractive term and dominates for weak electric charge
96 products or for small AP electrical mobilities (Figure 1, F) and is always attractive (due to the charge
97 distribution at the droplet surface with opposite sign to the AP charge). A detailed study of their
98 contribution can be found in Tinsley and Zhou (2015) or Dépée et al. (2019).
99 Several laboratory studies investigated the influence of the electric charges on the CE (Beard, 1974;
100 Wang and Pruppacher, 1977; Lai et al., 1978; Barlow and Latham, 1983; Wang et al., 1983; Byrne and
101 Jennings, 1993; Lemaitre et al., 2020) – summarised in Table 1. However, most of these works have
102 faced difficulties in controlling all parameters impacting the CE. For instance, Beard (1974) did not
103 measure the AP charge; Lai et al. (1978) used a polydispersed AP size distribution, the relative
104 humidity level was not provided and the terminal velocity of the droplets was not reached ; Barlow
105 and Latham (1983) used a polydispersed AP size distribution and the relative humidity level
106 significantly varied from 50 to 70 % in their measurements; in the work of Byrne and Jeannings (1993)
107 the droplet velocity does not reach the terminal velocity; the relative humidity measured in Lemaitre
108 et al. (2020) varied from 27 and 37 %. For these reasons, it is really difficult to find comparable CE
109 measurements in the literature as Barlow and Latham (1983) concluded after highlighting a

discrepancy of few orders of magnitude between all these authors. Nevertheless, Wang and Pruppacher (1977) and Wang et al. (1983) succeeded in controlling the charges and the sizes (as well as the relative humidity for Wang and Pruppacher (1977) but they considered only unlike signs between both droplets and APs. In their study, Lemaitre et al. (2020) did not observed any influence of electric charges on CE since for the low relative humidity level and the large droplet radius considered, the diffusiophoretis and thermophoresis dominated the AP collection.

Thus, only the Coulomb inverse square term in the analytical expression of the electrostatic forces can be documented whereas the contribution of the short-range attractive term has not been experimentally verified until now.

Table 1 Laboratory studies focused on the influence of electric charges on the CE. Charges are presented in number of elementary charges.

Parameter / Study	Droplet radius (µm)	AP radius (µm)	Droplet charge ($|e|$)	AP charge ($|e|$)	Relative humidity (%)	Terminal velocity
Beard (1974)	200 - 425	Monodispersed 0.35-0.44 ± 0.04	10^4 - 10^6	**Not measured**	99	Reached
Wang and Pruppacher (1977)	170 - 340	Monodispersed 0.25 ± 0.03	10^6	9 & 15 ± 2	23 ± 2	Reached
Lai et al. (1978)	620 & 820	**Polydispersed** 0.15 - 0.45	10^7 - 10^8	**Not measured**	**Neither controlled nor measured**	**Not reached**
Barlow and Latham (1983)	270 - 600	**Polydispersed** 0.2 - 1	10^4 - 10^7	Neutralised	**Uncontrolled but measured** 50 - 70	Reached
Wang et al. (1983)	69 - 250	Monodispersed 0.038 - 0.1	10^7 - 10^8	**1 – 13.5**	**Uncontrolled**	Reached
Byrne and Jennings (1993)	400 - 500	Monodispersed 0.35 - 0.88	10^5 - 10^8	360 - 750	57	**Not reached**
Lemaitre et al. (2020)	1275	**Polydispersed** 0.15 and 0.25	10^5 - 10^8	Neutralised and measured (0 ± 0.1)	**Uncontrolled** but measured 27 - 37	Reached

The purpose of this study is to overcome this lack of data by providing new CE measurements for weakly and strongly droplets and APs charges with both negative and positive charge products, to quantify the effect of the short-range attractive term on the CE since its contribution was previously predicted by modelling (Tinsley and Zhou, 2015; Dépée et al., 2019).

Thus, a novel experiment has been designed to study the influence of electric charges on the CE which is presented in this paper. Note that this experiment was also used to study the influence of relative humidity which is the object of the companion paper: Part I **(Dépée et al., 2020)**.

The first part of the paper describes the experimental setup. Afterwards, the method to evaluate the CE and the uncertainties are detailed. Then, the measurements are presented and confronted with the prediction of Kraemer and Johnstone (1955) and the Lagrangian model of Dépée et al. (2019). Finally, this work concludes with the experimental validation of the Dépée et al. (2019) model

134 and a necessary incorporation of the modelled CEs in cloud models, pollution models, climate models,
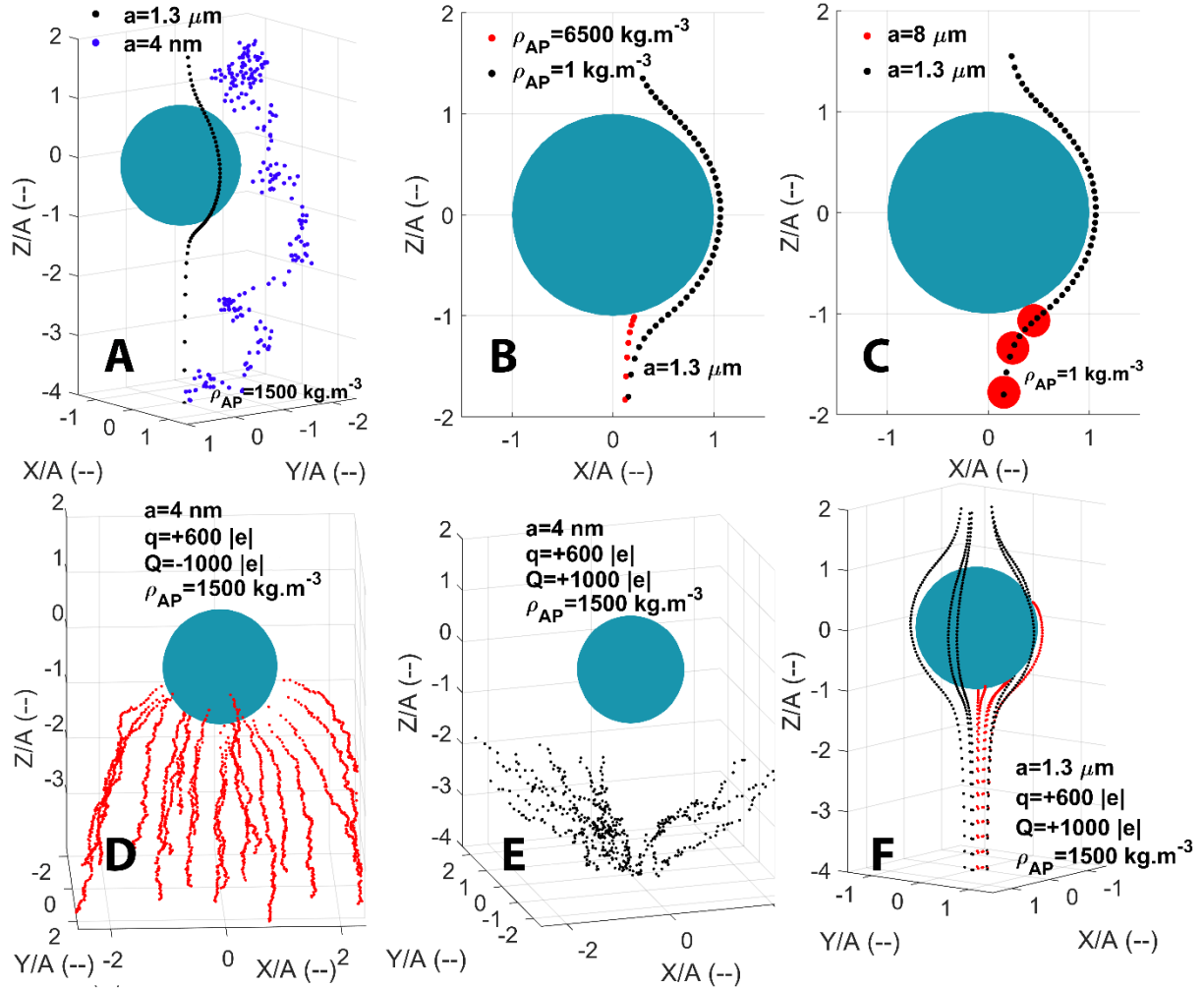135 and so forth, to study the "electroscavenging".

136
137 Figure 1 APs trajectories computed with the extended Dépée et al. (2019) model for a 50 μm droplet
138 radius (A) and AP with various radii (a) and densities (ρ_{AP}). The air temperature (T_{air}) and the air
139 pressure (P_{air}) are respectively -17°C and 540 hPa. The panels indicate the effects of Brownian
140 motion (A), inertial impact (B), interception (C), electrostatic forces with attractive (D) and repulsive
141 (E, F) Coulomb forces. Red trajectories result in an AP collection. The droplet (Q) and AP (q) charges
142 are labelled. In Figures 1 B to F - the red trajectories result in an AP collection. Adapted from Part I
143 (**Dépée et al., 2020**).

144
145
146 **1   EXPERIMENTAL SETUP**
147 **1.1   Overview**
148 Figure 2 shows the In-Cloud Aerosol Scavenging Experiment (In-CASE) which has been built to study
149 the influence of the electric charges on the CE. Droplets fall at their terminal velocity (≈25 cm/s)
150 into a chamber through an AP flow of 1.5 l/min. The flow velocity is 1.3 cm/s and the AP transfer
151 time in the collision chamber is almost 80 s. The In-CASE's chamber is subdivided into 3 parts - the
152 injection head where droplets and APs are inserted; the collision chamber where droplets and APs
153 interact with each other; the aerodynamic separator set at the bottom's chamber impacts droplets
154 into an impaction cup while uncollected APs pass out of the chamber toward a High Efficiency
155 Particulate Air (HEPA) filter. For this latter stage, an Argon updraft assures that there are no AP that
156 settle into the droplet impaction cup. More details on the In-CASE's chamber can be found in section
157 1.2 of **Dépée et al. (2020)**.
158 APs are atomised from a sodium fluorescein salt solution ($C_{20}H_{10}Na_2O_5$). This molecule has been
159 used for its significant fluorescent properties, detectable at very low concentrations (down to 10^{-10}
160 g/l). Once generated, the APs flow through a diffusion dryer and a portion of the flow is then directed
161 into a Differential Mobility Analyser (DMA; TSI 3080) to select APs following their electrical mobilities

whereas the overflow ends in an exhaust (black, Figure 2). At the DMA's outlet, the AP size distribution is assumed to be monodispersed (discussed in section 2.1). Thereafter, APs are electrically charged by a custom-designed field charger (section 1.4). Since the optimised AP flowrate in the charger is 1.5 l/min and the maximum AP flowrate in the DMA was 1.2 l/min during the experiments, a clean air flowrate is added at the charger's inlet. Before the AP injection in the In-CASE's chamber, the flow is humidified to ensure a high relative humidity level inside the collision chamber (section 1.2). Thus, the hygroscopicity of the sodium fluorescein salt is considered during the experiments (see section 2.2). Before the AP collection on the HEPA filter, the APs flow through a low-energy X-ray neutraliser (< 9.5 keV, TSI 3088) to eliminate charge accumulation on this filter leading to AP deposition on the metallic walls of the filter holder. Note that the pipes are anti-static and connected to the ground (as well as the collision chamber) so there is no accumulation charge before the HEPA filter due to AP deposition.

Droplets are generated with a piezoelectric injector provided by Microfab (MJ-ABL-01 model) with an internal diameter of 150 μm - at 25 Hz to prevent droplets from coalescencing. The generator is set in a housing made with a 3D printer which is located in the injection head (Figure 5, Right). An electrostatic inductor is also placed in the housing to charge droplets (section 1.5). The droplet size is measured during experiments by optical shadowgraphy (with a strobe and a camera, Brown in Figure 2) through two facing windows in the injection head. Further details can be found in section 1.4 of **Dépée et al. (2020)** but note that the size distributions of the droplets generated by the piezoelectric injector are considered monodispersed since the droplet size dispersion is very low ($\sigma \sim 1\%$).
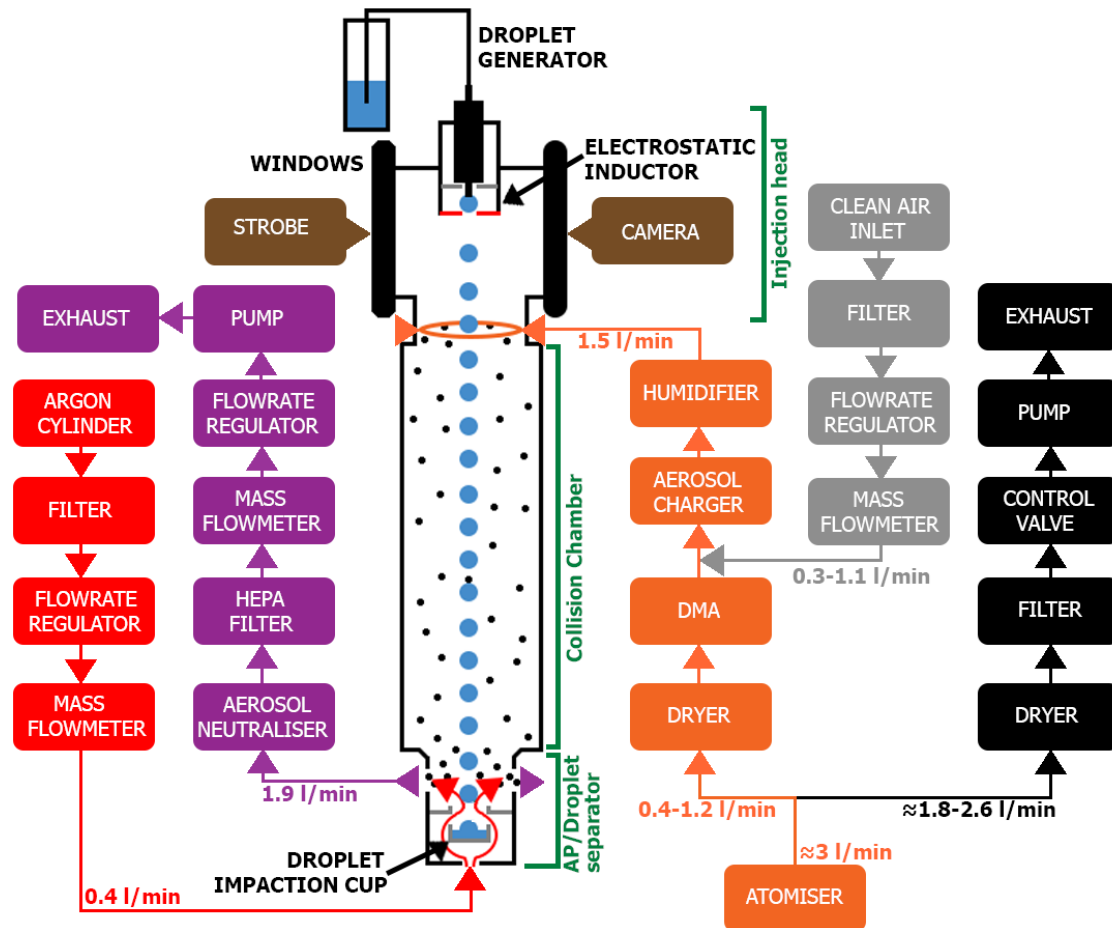
Figure 2 In-CASE setup to study the electric charges' influence - adapted from Part I (**Dépée et al., 2020**). Colors represent different functions. Red – upward argon flow against AP pollution in the droplet impaction cup. Purple – AP (and Argon) evacuation toward the HEPA filter after neutralisation. Orange – AP, generation, selection and charging. Black – surplus evacuation and DMA flowrate control. Grey – clean air adding for a constant flowrate at the AP charger's inlet. Brown – droplet radius measurement.

1.2   Thermodynamic conditions in the In-CASE's chamber

192 Thermodynamic conditions were set as constant as possible during experiments to get comparable
193 CE measurements. The pressure in the In-CASE's chamber was one atmosphere and the mean
194 temperature for the campaign presented in this paper was $1.08 \pm 0.12\,°C$. As referred in section 1.2
195 of **Dépée et al. (2020)**, the chamber's temperature is controlled through a cooling system which
196 indirectly sets the relative humidity level in the chamber. Here, the temperature of the pure water
197 in the humidifier placed before the In-CASE's chamber (Figure 2) was increased to get a mean relative
198 humidity level in the chamber of $95.1 \pm 0.2\,\%$. Note that this relative humidity level was the maximum
199 which could be reached with In-CASE. In this way, the contribution of the thermophoretic and the
200 diffusiophoretic effects in the CE measurements were reduced as much as possible.
201
202 **1.3   Droplet evaporation**
203 The droplet evaporation was theoretically evaluated through the section 13.2 of Pruppacher and Klett
204 (1997). The terminal velocity of the droplet ($U_{A,\infty} \approx 25$ cm/s) is computed from Beard (1976)
205 meanwhile the droplet residence time in the collision chamber (≈ 4 s) is deduced from the changes in
206 droplet radius and terminal velocity. For a relative humidity level of 95 %, it was found that the
207 droplet radius decreases by less than 0.3 % from the droplet generation to the bottom of the collision
208 chamber. Thus, the droplet evaporation in the In-CASE collision chamber was neglected for the
209 discussions below.
210
211
212
213 **1.4   AP charging**
214 APs are electrically charged by passing through a custom-designed field charger adapted from Unger
215 et al. (2004). The scaled geometry is presented in Figure 3. This charger is based on a system of
216 electric discharges produced between a high potential tungsten wire and a grounded cylinder. A
217 metallic converging portion is used at the charger's outlet to trap ions and ensure only charged APs
218 can leave the charger. A Teflon ball (∅=1 mm) is set at the end of the tungsten wire to ensure there
219 is no point effect between the wire and the ion trap. A large number of ions are then created and
220 migrate between the two centimeters interelectrode space along the electric field lines. Finally, the
221 APs flow through them and are charged by ion attachment.
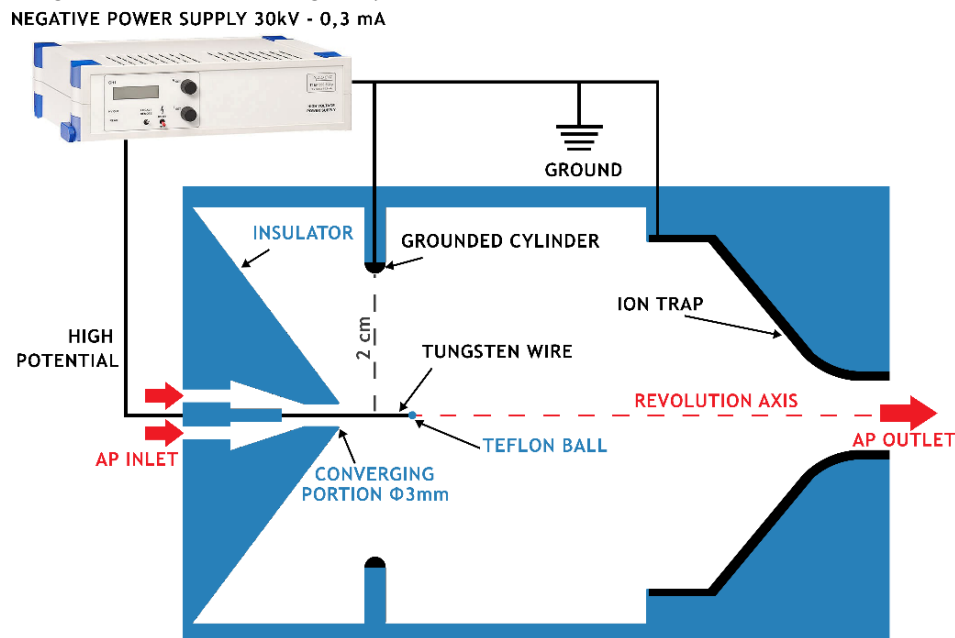
222
223
224 Figure 3 Geometry of the home-made AP charger based on Unger et al. (2004) (at scale).
225
226 The charging relationships of the charger used during all experiments are presented in Figure 4. They
227 provide the mean electric AP charge related to the potential at the tungsten wire for the 4 AP radii
228 considered here. It results from *ex situ* experiments which are detailed in Appendix A. Note that APs
229 are negatively charged through the discharge regime used (negative Trichel regime) and there is an
230 electric potential where the AP charge saturates which is typical for field chargers (Pauthenier and
231 Moreau-Hanot, 1932). These results were performed at an AP flowrate of 1.5 l/min which was found

232 to maximise the AP penetration inside the charger and consequently the AP concentration inside the
233 In-CASE's chamber. Penetration tests - not presented in this study - were deduced by varying the AP
234 flowrate in the setup detailed in Appendix A.

235
236
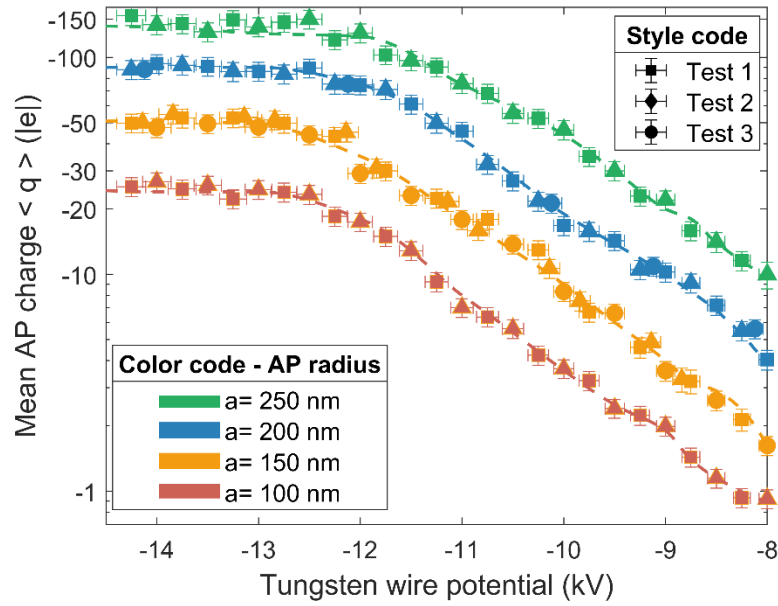
237 Figure 4 AP charging relationships used during experiments for the 4 AP radii (a) considered. Error
238 bars represent the standard deviations in measurements.

239

1.5   Droplet charging

241 The droplets charge is controlled through an electrostatic inductor adapted from Reischl et al. (1977).
242 Two parallel metallic plates are set at the droplet generator's nozzle (Figure 5, left) - one plate
243 connected to the neutral potential and the other one to a potential referred as V_{ind}. It induces an
244 electric field ($E_{ind} \sim 10^2$-10^3 V/m) at the nozzle. Since sodium chloride is added to the pure water that
245 feeds the piezoelectric droplet generator, this electric field can selectively attract negative or
246 positive ions toward the nozzle where the droplet is formed, according to its sign. If V_{ind} is negative,
247 the positive sodium ions (Na^+) migrate toward the nozzle and the negative chloride ions (Cl^-) are
248 repulsed from the nozzle and inversely if the potential is positive. Furthermore, the amplitude of the
249 electric field (E_{ind}) sets the ion quantity in the droplet. Note that the sodium chloride concentration
250 has no impact on the induced droplet charge if the ion number is large enough for the entire
251 experiment time (Reischl et al., 1977) - 3.3 g/l was used here.

252

253
254

Figure 5 (**Left**) Electrostatic inductor below the piezoelectric droplet generator. (**Center**) Cross section of the housing made with a 3D printe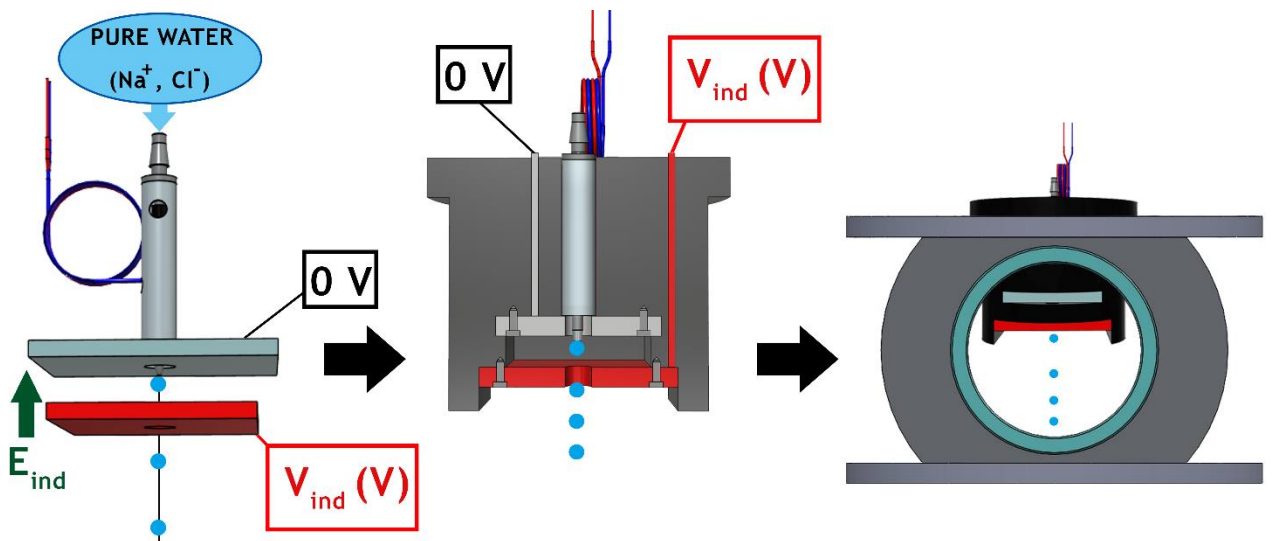r that hold the droplet generator. (**Right**) Injection head at the top of the In-CASE's chamber containing the housing made with a 3D printer.

A method to evaluate the droplet charge was developed in this study and is detailed in Appendix B. In Figure 6, the resulting charging relationship of the electrostatic inductor is presented. It gives the droplet charge (Q) as a function of the electrostatic inductor potential (V_{ind}). We note that the droplet generator produces highly electrically charged droplets since the droplet charge is evaluated to about -8,400 elementary charges, for a zero potential at the inductor plate (V_{ind}= 0 V). This is in line with Ardon-Dryer et al. (2015) which used a similar generator and measured up to 10^4 elementary charges on the generated droplets. Finally, this charging relationship is used during experiments to positively or negatively set the droplet charges. The electrostatic inductor and the droplet generator are placed into a housing made with a 3D printer (Figure 5, center), this latter being placed in the injection head at the top of the In-CASE's chamber (Figure 5, right).
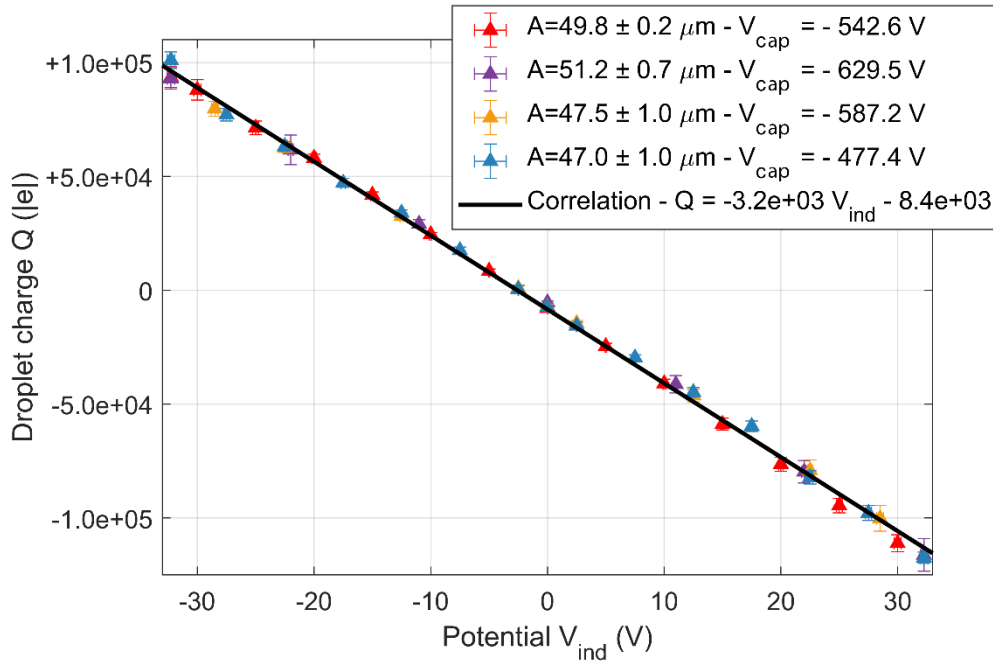
Figure 6 Droplet charge versus electrostatic inductor voltage. The colours identify different tests performed to ensure there is no droplet charge modification over time and manipulations. Error bars represent the standard deviation of the droplet radii evaluated. The parameter V_{cap} is the potential at the capacitor to measure the droplet charge. Note that the radius of the droplet is deduced from the reversed Beard (1976) model and its terminal velocity – this latter being measured by optical shadowgraphy. See Appendix B for more further details.

2 DATA ANALYSIS

2.1 Assumption of a monodispersed AP size distribution

As a reminder, APs flow through a DMA (Figure 2) to select APs following their electrical mobility. As explained in section 2.2 of the Part I (**Dépée et al., 2020**), several AP radii can actually be selected depending on their elementary charges given that they have the same electrical mobility. For example, with a selected AP radius of 100 nm at the DMA (considering one elementary charge on it), the doubly-charged AP radii of 161.8 nm will also be selected.

Sometimes, the multiple charged APs cannot be neglected in the AP flow at the DMA's outlet. The CE deduction is then more difficult (**Dépée et al., 2020**). Here, the aerodynamic impactor at the DMA's inlet as well as the AP flowrate in the DMA were optimised to prevent double (and greater) charged AP from being selected by the DMA. Indeed, the cut-off radius of the impactor at the DMA's inlet (referred as $D_{50\%}/2$) - which is the radius where 50 % of the APs are impacted - is small enough

293 compared to the double charged AP radius. This is summarised in Table 2 for all selected AP radii
294 used in the experiments. Thus, the AP size distribution at the DMA's outlet is assumed to be
295 monodispersed and the CE is deduced as follows.
296 Table 2 AP selection parameters

Selected dry AP radius by the DMA (single charged)	Double charged dry AP radius with the same electrical mobility	AP flowrate in the DMA	Cut-off radius of the impactor at the DMA's inlet ($D_{50\%}/2$)
100 nm	161.8 nm	1.2 l/min	140 nm
150 nm	253.7 nm	1.0 l/min	157 nm
200 nm	348.3 nm	0.6 l/min	213 nm
250 nm	444.3 nm	0.4 l/min	268.5 nm

297
298 **2.2 Collection efficiency definition**
299
300 The collection efficiency (CE) is calculated from the equation (1):

$$CE(a, A, q, Q, HR) = \frac{m_{AP,d}}{m_{AP,available}} \tag{1}$$

301 Where $m_{AP,d}$ is the AP mass collected by all droplets which is directly measured by fluorescence
302 spectrometry analysis of the droplets collected in the impaction cup, which is located at the bottom
303 of the In-CASE chamber (Figure 4 of **Dépée et al., 2020**). $m_{AP,available}$ is the mass of available APs in
304 the volume swept by all droplets - evaluated with the equation (2) :

$$m_{AP,available} = \pi(A + GroF(RH) \times a)^2 \times F_d \times \Delta t \times H_{eff} \times C_{m,AP} \tag{2}$$

305 With A - the droplet radius, F_d - the droplet generation frequency, Δt - the experiment duration (from
306 3 to 6 hours), a - the AP dry radius, $C_{m,AP}$ – the mean AP mass concentration in the In-CASE collision
307 chamber, $GroF$ - the growth factor of AP depending on the relative humidity (RH). This latter
308 characterises the hygroscopicity of the sodium fluorescein salt - further details related to its
309 evaluation can be found in section 1.2.3.3 of **Dépée et al. (2020)**. H_{eff} is the effective height of
310 interaction between APs and droplets calculated with the equation (3):

$$H_{eff} = \frac{U_{A,\infty}}{U_{A,\infty} + V_Q} H_{In-CASE} \tag{3}$$

311 With the AP flow velocity (V_Q) equal to 1.3 cm/s (for an AP flowrate of 1.5 l/min), the droplet
312 terminal velocity ($U_{A,\infty}$) assumed to be equal to 25 cm/s and the In-CASE collision chamber's height
313 ($H_{In-CASE}$) of 1 meter.
314
315 In equation (2), the mean AP mass concentration ($C_{m,AP}$) in the In-CASE collision chamber is evaluated
316 from the fluorescence spectrometry analysis of the HEPA filter. It is given by the equation (4) where
317 $Q_{In-CASE,c}$ is the AP flowrate going through the In-CASE collision chamber and $m_{AP,tot}$ is the total AP
318 mass on the HEPA filter at the end of the experiment.
319

$$C_{m,AP} = \left(1 + \frac{1 - P_{InCASE,a,q}}{2}\right) \frac{m_{AP,tot}}{\Delta t \times Q_{In-CASE,c}} \tag{4}$$

320 The mean AP mass concentration is corrected considering the penetration ($P_{InCASE,a,q}$) in the collision
321 chamber which depends on the AP radius (a) and charge (q). This parameter was estimated during
322 *ex situ* experiments where the setup was the same as Figure 2, the only difference being a
323 Condensation Particle Counter (CPC) set after the AP neutraliser and the AP charger to measure two
324 AP number concentrations - 1 and 2, respectively. The penetration is then defined as concentration
325 1 over concentration 2. Thus, the measured penetration accounts for the AP deposition due to

electrostatic forces on the wall of the collision chamber as well as in the pipes from the AP charger to the HEPA filter and the humidifier (Figure 2). The measured penetrations are presented in Table 3. It is observed the penetration decreases when the AP charges (q) increases and the AP radius (a) decreases since the electrical mobility of APs is larger. During experiments, the AP number concentration was ranged from 3.10^4 cm^{-3} (for a=100 nm and $q = -10 \pm 1$ $|e|$) to 2.10^3 cm^{-3} (for a=250 nm and $q = -90 \pm 9$ $|e|$). As a reminder, the pipes are anti-static and connected to the ground (as well as the collision chamber) so there is no charge accumulation due to AP deposition during experiments. Thus, the penetrations presented in Table 3 are assumed to be constant over time. Note that the AP deposition was neglected in Part I (**Dépée et al., 2020**) since the penetration was almost 100 % when the APs are neutralised.

Table 3 Measured penetration for the experimental conditions.

Dry AP radius (a)	AP charge (q)	Penetration ($P_{InCASE,a,q}$)
100 nm	-10 ± 1 $|e|$	94.7 %
	-20 ± 2 $|e|$	86.0 %
150 nm	-11 ± 1 $|e|$	96.5 %
	-30 ± 3 $|e|$	86.2 %
200 nm	-10 ± 1 $|e|$	97.0 %
	-34 ± 3 $|e|$	88.8 %
	-71 ± 7 $|e|$	78.2 %
250 nm	-22 ± 2 $|e|$	94.1 %
	-52 ± 5 $|e|$	89.6 %
	-90 ± 9 $|e|$	81.8 %

2.3 Uncertainties

The relative CE uncertainty (u_{CE}) is calculated following Lira (2003) and presented in equation (5):

$$u_{CE} = \sqrt{u_A{}^2 + u_{H_{eff}}{}^2 + u_{N_d}{}^2 + u_{m_{AP,d}}{}^2 + u_{C_{m,AP}}{}^2} \qquad (5)$$

Where the relative uncertainties are related to the droplet radius ($u_A \approx 1\%$), the effective height of interaction between droplets and APs ($u_{H_{eff}} \approx 4\%$), the number of injected droplets during the experiment ($u_{N_d} \approx 2\%$), the measured AP mass in the droplet impaction cup ($u_{m_{AP,d}}$) and the mean AP mass concentration in the In-CASE collision chamber during the experiment ($u_{C_{m,AP}}$).

The relative uncertainty $u_{m_{AP,d}}$ is evaluated through the equation (6) :

$$u_{m_{AP,d}} = \sqrt{u_{fluorimeter}{}^2 + u_{dilution}{}^2} \qquad (6)$$

Where $u_{dilution}$ is the relative uncertainty of the dilution performed during the spectrometry analysis, assumed to be equal to 1 %, and $u_{fluorimeter}$ is the relative uncertainty of the fluorimeter which can be up to 30 % when the measured AP mass is close to the detection limit. The relative uncertainty of the mean AP mass concentration in the In-CASE collision chamber ($u_{C_{m,AP}}$) is calculated through the equations (7) :

$$\begin{cases} u_{C_{m,AP}} = \sqrt{u_{m_{AP,tot}}^2 + u_{Q_{In-CASE,c}}^2 + u_{\Delta t}^2 + u_P^2} \approx \sqrt{u_{m_{AP,tot}}^2 + u_{Q_{In-CASE,c}}^2 + u_P^2} \\ u_{m_{AP,tot}} = \sqrt{u_{fluorimeter}^2 + u_{dilution}^2} \end{cases} \quad (7)$$

$u_{m_{AP,tot}}$ is the relative uncertainty of the measured AP mass on the HEPA filter which depends on the relative uncertainties of the dilution ($u_{dilution} \approx 1\%$) and the fluorimeter ($u_{fluorimeter} \leq 30\%$) - $u_{Q_{In-CASE,c}}$ is the relative uncertainty of the AP flowrate in the collision chamber equal to 1 % - $u_{\Delta t}$ is the relative uncertainty of the experiment duration which is neglected here. More details are addressed in Part I, section 2.3 (**Dépée et al., 2020**) where the same definitions are used, except the relative uncertainty of the AP penetration in the collision chamber (u_P) is added here (equation (8)).

$$u_P = \frac{1 - P_{InCASE,a,q}}{2} \quad (8)$$

As mentioned in 3.2.3.2, an AP pollution independent from the experiment (pollution during the spectrometry analysis, when the droplet impaction cup is extracted at the end of experiments, etc.) remains and should be considered in equation (5). Indeed, it can significantly increase the CE measurement, especially when the measured AP mass is close to the detection limit. It means, when the CE is below 10^{-4} for the experiment durations considered in the study. Instead of omitting this uncertainty which is difficult to evaluate, the low uncertainty for the CE measurements below 10^{-4} were increased until the end of the axis in Figure 7 and 10.

Also, we assume the APs have the same charge (q). Actually, it exists an AP charge distribution which, even slightly dispersed, can affect the CE measurement. Nevertheless, the AP charge distribution was not measured here.

3 RESULTS AND DISCUSSIONS

3.1 Extension of the Dépée et al. (2019) model

CE measurements are compared to the model of Dépée et al. (2019) which models the electrostatic forces (F_{elec}) between droplets and APs in the CE calculation. Since all experiments were performed in subsaturated air ($RH = 95.1 \pm 0.2$ %), the thermophoretic (F_{th}) and the diffusiophoretic (F_{df}) forces were also considered for the comparison with the model. Indeed, **Dépée et al. (2020)** showed that the contribution of these two effects is significant even though the relative humidity is close to 100 %. Thus, the Dépée et al. (2019) model is extended here by replacing the resulting velocity at the AP location ($\boldsymbol{U_{f@p}}^*$ in their Equation 6) by the equation (9):

$$\boldsymbol{U_{f@AP}}^*(t) = \boldsymbol{U_{f@AP}}(t) + \frac{\tau_{AP}}{m_{AP}}\left(\boldsymbol{F_{buoy}} + \boldsymbol{F_{df}} + \boldsymbol{F_{elec}} + \boldsymbol{F_{th}}\right) \quad (9)$$

Where $U_{f@AP}$ is the fluid velocity at the AP location, τ_{AP} the AP relaxation time and m_{AP} the AP mass. The expression of the buoyancy force (F_{buoy}) is detailed in equation system (B.1), F_{df} and F_{th} in the equations (12) of **Dépée et al. (2020)**. F_{elec} is defined in equation (10) :

$$\boldsymbol{F_{elec}} = \frac{q^2}{4\pi\varepsilon_0 A^2}\left[\overbrace{\left(-\frac{r^*}{(r^{*2}-1)^2} + \frac{1}{r^{*3}}\right)}^{Short-range\ attractive\ term} + \underbrace{\frac{1}{r^{*2}} \times \frac{Q}{q}}_{Coulomb\ inverse\ square\ term}\right]\boldsymbol{u_r} \quad (10)$$

With ε_0 - the permittivity of the free space, $\boldsymbol{u_r}$ - the unit vector in the radial direction from the droplet centre to the AP centre, r^* - the distance between the AP and droplet centres, normalised by the droplet radius A.

Note that radioactive APs are known to get positively charged (Clement and Harrison, 1992) whereas the APs were negatively charged in this work (Figure 4), through the charging regime used in the AP charger (for integrity of the tungsten wire over time). Nevertheless, since we have the relation $F_{elec}(q, -Q) = F_{elec}(-q, Q)$ in equation (10), the CE measurements with the same $\frac{q}{Q}$ ratios are equivalent, assuming this analytical expression is validated by the measurements (see section 3.2.3).

3.2 Collection efficiency measurements

The CE measurements for various charges are presented in Table 4 for the 4 wet AP radii (a_{wet}) considered in this study. Note that the wet AP radii are the ones of the APs which grew in the collision chamber due to their hygroscopicity. During experiments, the AP radius increases by a growth factor ($GroF$) between 1.73 and 1.75 (since we actually considered the 4 mean levels of relative humidity for the 4 AP radii used in the experiments). Further details related to the calculation of the growth factor can be found in section 1.2.3.3 of Dépée et al. (2020). In Table 4, the droplet (Q) and AP (q) charges are also informed by number of elementary charges. The mean temperature was 1.08 ± 0.12°C and the mean relative humidity was 95.1 ± 0.2 % for a droplet radius of 48.5 ± 1.1 μm. Note that the wet AP density depends on the one of sodium fluorescein salt and water. The equation (1) of **Dépée et al. (2020)** yielded a density of 1110 kg.m^{-3}. The key features of the experiments are summarised in Table 5.

Table 4 CE measurements

a_{wet} (nm) \ $Q(|e|)$; $q(|e|)$	$9.6 \times 10^4 \pm 4.3 \times 10^3$	$3.0 \times 10^4 \pm 1.9 \times 10^3$	$5.0 \times 10^3 \pm 8.4 \times 10^2$	$0 \pm 6.0 \times 10^2$	$-5.0 \times 10^3 \pm 7.7 \times 10^2$	$-1.0 \times 10^4 \pm 8.7 \times 10^2$	$-3.0 \times 10^4 \pm 1.4 \times 10^3$
175 ± 3 ; -10 ± 1	3.91×10^{-2}	2.44×10^{-2}	3.47×10^{-3}	4.17×10^{-3}	5.58×10^{-3}	9.81×10^{-4}	2.55×10^{-4}
175 ± 3 ; -20 ± 2	6.77×10^{-2}	3.47×10^{-2}	6.99×10^{-3}	5.07×10^{-3}	4.25×10^{-3}	9.17×10^{-4}	4.12×10^{-5}
260 ± 3 ; -11 ± 1	2.41×10^{-2}	1.30×10^{-2}	3.25×10^{-3}	2.97×10^{-3}	2.14×10^{-3}	1.34×10^{-3}	1.93×10^{-4}
260 ± 3 ; -30 ± 3	7.91×10^{-2}	2.31×10^{-2}	7.96×10^{-3}	5.75×10^{-3}	3.47×10^{-3}	2.57×10^{-3}	4.97×10^{-5}
346 ± 4 ; -10 ± 1	2.24×10^{-2}	8.98×10^{-3}	3.03×10^{-3}	1.86×10^{-3}	1.84×10^{-3}	1.05×10^{-3}	5.20×10^{-4}
346 ± 4 ; -34 ± 3	4.58×10^{-2}	1.40×10^{-2}	5.39×10^{-3}	3.91×10^{-3}	2.90×10^{-3}	2.23×10^{-3}	3.60×10^{-5}
346 ± 4 ; -71 ± 7	9.17×10^{-2}	3.25×10^{-2}	1.70×10^{-2}	7.33×10^{-3}	5.51×10^{-3}	2.88×10^{-3}	2.21×10^{-5}
432 ± 5 ; -22 ± 2	3.74×10^{-2}	1.49×10^{-2}	3.22×10^{-3}	2.49×10^{-3}	1.85×10^{-3}	2.44×10^{-3}	1.25×10^{-4}
432 ± 5 ; -52 ± 5	7.62×10^{-2}	4.13×10^{-2}	1.13×10^{-2}	3.23×10^{-3}	3.23×10^{-3}	4.17×10^{-3}	1.06×10^{-4}
432 ± 5 ; -90 ± 9	1.77×10^{-1}	3.55×10^{-2}	1.83×10^{-2}	6.90×10^{-3}	4.75×10^{-3}	4.56×10^{-3}	2.43×10^{-5}

Table 5 Key features of the In-CASE setup

Feature	Numerical value
Collision chamber's parameters	
Height of the collision chamber ($H_{In-CASE}$)	1 m
Distance between droplet injection and AP injection	≈10 cm
Diameter of the collision chamber	5 cm
Impaction cup diameter	2.5 cm
AP flowrate in the DMA	Between 0.4 and 1.2 l/min (following the selected AP radius)
Clean air adding at the inlet of the aerosol charger	Between 0.3 and 1.1 l/min (following the selected AP radius)
AP flowrate in the aerosol charger	1.5 l/min

AP flowrate in the collision chamber ($Q_{In-CASE,c}$)	1.5 l/min
Flow velocity in the collision chamber (V_Q)	1.3 cm/s
Flowrate of the upward Argon at the inlet of AP/droplet separator	0.4 l/min
Flowrate of the upward Argon in the impaction cup	1.4 cm/s
AP and Argon flowrate at the outlet of In-CASE chamber (toward the HEPA filter)	1.9 l/min
Air pressure in the collision chamber (P_{air})	1 atm
Temperature in the collision chamber (T_{air})	$1.08 \pm 0.12\,°C$
Relative humidity in the collision chamber (RH)	95.1 ± 0.2 %
Duration of experiments (Δt)	From 3 to 6 hours (related to the expected APs mass in droplets)
AP's parameters	
Selected dry AP radius during experiment (a)	100, 150, 200 or 250 nm
Growth factor of the APs ($GroF$)	Between 1.73 and 1.75 (following the mean levels of relative humidity for the 4 separated AP radii)
Density of sodium florescein ($\rho_{fluorescein}$)	1580 kg.m^{-3}
Density of the wet APs (ρ_{AP})	≈1110 kg.m^{-3}
AP terminal velocity	≤10^{-3} cm/s (equal to 8x10^{-4} cm/s for the larger selected dry AP radius 250 nm)
AP residence time in the collision chamber	≈80 s
Total AP concentration (single and multiple charged at the DMA's outlet)	From 3.10^4 cm^{-3} (for a=100 nm and $q = -10 \pm 1$ $\|e\|$) to 2.10^3 cm^{-3} (for a=250 nm and $q = -90 \pm 9$ $\|e\|$)
AP charge (q)	From -10 ± 1 to -90 ± 9 elementary charges (following the selected AP radius)
Droplet's parameters	
Droplet radius (A)	48.5 ± 1.1 µm
Droplet generation frequency (F_d)	25 Hz
Droplet terminal velocity ($U_{A,\infty}$)	≈25 cm/s
Number of injected droplets during experiments (N_d)	From 270,000 to 540,000 (related to the expected APs mass in droplets)
Observed distance between two successive droplets	≈ 9 mm ≈ 180 droplet radii
Droplet residence time in the collision chamber	≈4 s
Droplet charge (Q)	From $-3.0 \times 10^4 \pm 1.4 \times 10^3$ to $9.6 \times 10^4 \pm 4.3 \times 10^3$ elementary charges
Droplet charge after neutralisation (Q)	0 ± 600 elementary charges

Droplet evaporation between the injection and the end of the collision chamber	≈0.3 %
Sodium chloride concentration in the pure water	3.3 g/l

423
424
425 ### 3.2.1   Effect of the product of the droplet and AP charges on the collection efficiency
426
427 The CE measurements for a wet AP radius of 432 nm are presented in Figure 7 as a function of the
428 product of the droplet (Q) and AP (q) charges. The measurements are compared to the Dépée et al.
429 (2019) extended model (solid line) for the 4 AP charges, considering the AP and droplet charge
430 uncertainties. There is a good agreement between model and measurements which indicates that
431 the analytical expression of the electrostatic forces (equation (10)) reliably describes the
432 observations.
433 Indeed, an important charge influence is measured, increasing or decreasing the CE up to two orders
434 of magnitude for large negative or positive charge products, respectively, compared to the
435 theoretical CE value disregarding the electrostatic effects (dashed line in Figure 7). This is due to
436 the Coulomb inverse square term in the electrostatic forces' equation (10) which dominates -
437 attracting or repelling the APs from the droplet depending on whether the AP and droplet charges
438 have unlike or like signs.
439 For small positive charge products (approximately $0 \leq q \times Q \leq 10^6 \, |e| \times |e|$), an increase of CE with
440 a factor of more than three is measured compared to the theoretical CE value without electrostatic
441 forces. This fact truly emphasises the contribution of the short-range attractive term in equation (10)
442 which attracts the APs toward the droplet even though the droplet and AP charges have like signs.
443 Indeed, as previously stated, this term prevails for small charge products (Dépée et al., 2019).
444
445 Note that the same influence of the charge product on the CE is observed for the other three wet AP
446 radii – the CE varies up to four orders of magnitude.
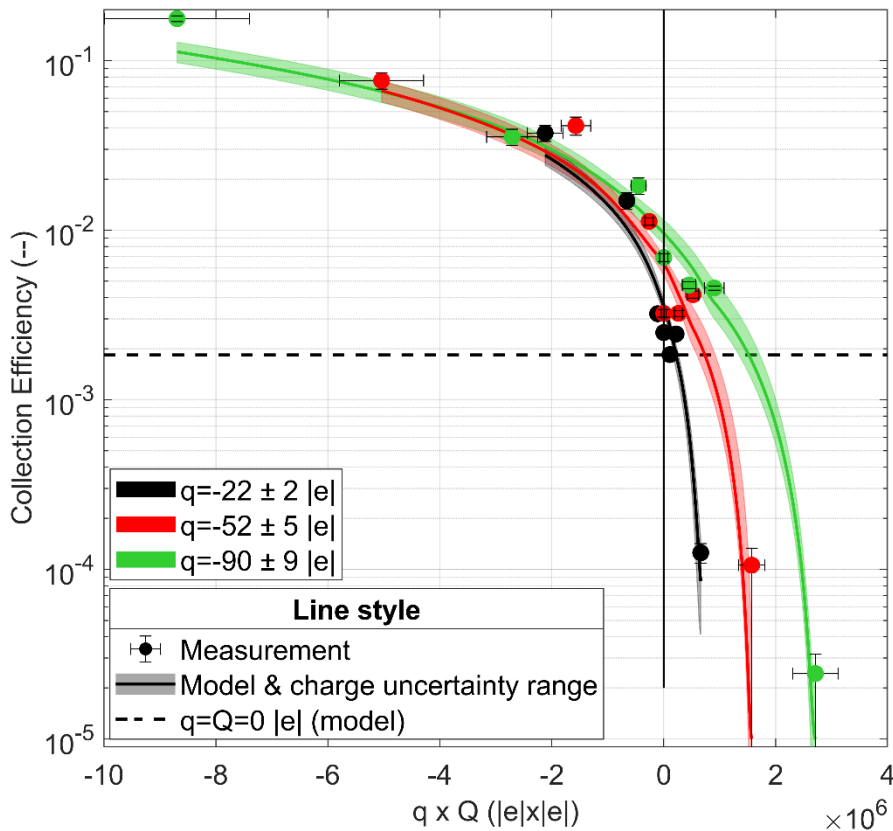447

448
449 Figure 7 CE measurement as a function of the product of the droplet (Q) and AP (q) charges for the
450 wet AP radius of 432 nm and a droplet radius of 48.5 ± 1.1 μm. The experimental conditions are
451 summarised in Table 5. Color code informs about the AP charge. The dashed line represents the

theoretical CE value disregarding the electrostatic forces (given the air parameters 1°C, 1 atm, 95% of relative humidity). The solid line is the interpolation of the Dépée et al. (2019) extended model (with the charge uncertainty range) for the respective CE measurements at a given AP charge.

3.2.2 Effect of the AP charge on the collection efficiency for a neutral droplet

In Figure 8, the CE measurements (circle) for a neutral droplet ($Q = 0 \pm 600 \, |e|$) are presented for the 4 wet AP radii - referred by the color code - with the respective theoretical CE values (triangle). The dashed line represents the theoretical CE value without electrostatic forces.
Note that the contribution of the electrostatic forces seems insignificant for an AP charge of about -10 elementary charges and an AP radius of 346 nm and 260 nm as well as an AP of 432 nm with -20 elementary charges. Indeed, these measurements are very close to the theoretical ones with no consideration of electrostatic forces. Several microphysical effects have probably an equivalent contribution on the CE measurements such as electrostatic, thermophoretic and diffusiophoretic forces, in addition to AP diffusion, weight and inertia.
However, at a given AP radius, an increase of the CE is observed when the number of elementary charges on the APs is larger. As a reminder, this increase appears even though the droplet is neutral (or poorly charged considering the charge uncertainty of 600 elementary charges). For example, given an AP radius of 346 nm, the CE is multiplied by almost a factor 4 when the AP charge increases from -10 to -71 elementary charges. It highlights the contribution of the short-range attractive term in equation (10), showing the presence of a surface charge distribution on the droplet formed by the partial influence of the AP electrostatic field on it. In the current case, this is the only contribution since the droplet is neutral and the Coulomb inverse square term is zero in equation (10). This is an important result since, to our knowledge, there is no experimental observation of the short-range attractive term on the CE in the previous studies of the literature. Here, the good agreement between measured (circle) and modelled (triangle) CEs confirms that the analytical expression of the short-range attractive term in equation (10) is reliable.
For a given AP charge, an increase of the CE is measured when the AP radius decreases, probably due to the increase of the electrical mobility of APs. This is in line with the numerical results of Dépée et al. (2019) even though electrostatic effects are not the only contribution involved in this CE increase. Indeed, the Brownian motion of the APs increases for smaller APs and enhances the collision between the droplet and APs.
Moreover, the curve slope could be increased for a decrease of the AP radius since the electrical mobility increases but this trend is not visible in Figure 8. It can be due to the uncertainties on the CE measurements, the droplet neutralisation and the AP charge.
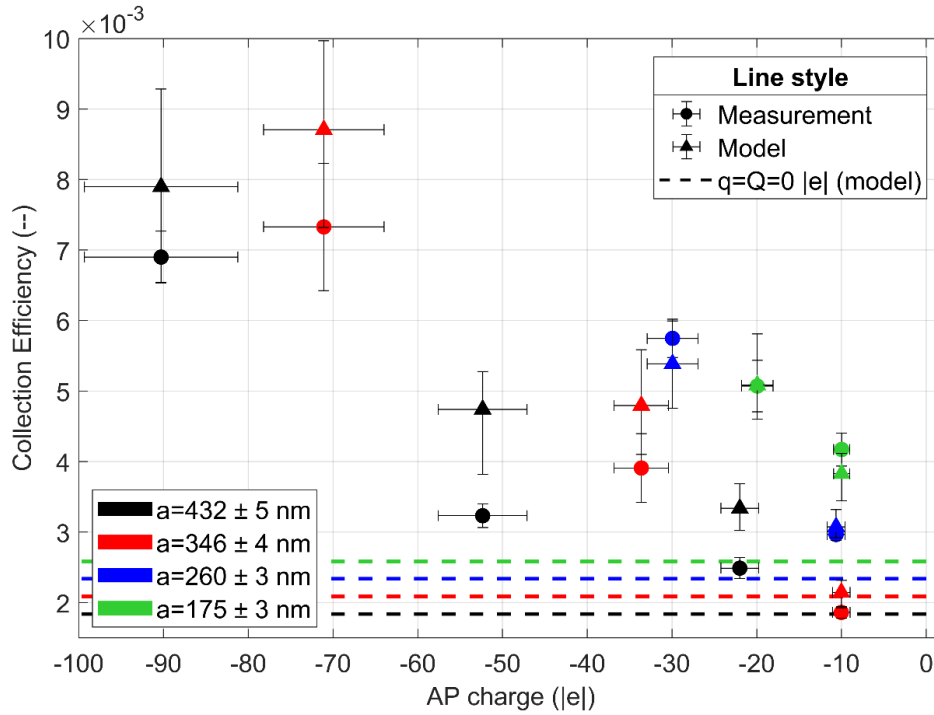
Figure 8 CE measurement (circle) as a function of the AP charge (q) for the 4 wet AP radii (Color code). The respective modelled CEs are also presented (triangle). The droplet is neutral with a radius of 48.5 ± 1.1 μm. The experimental conditions are summarised in Table 5. The dashed line represents the theoretical CE value disregarding the electrostatic forces (given the air parameters 1°C, 1 atm, 95% of relative humidity). The vertical error bars for the modelled CEs consider the AP and droplet charges uncertainties.

3.2.3   Comparison with existing models

3.2.3.1 Kraemer and Johnstone (1955) prediction

To describe the impact of the electric charges on the CE, there is the well-known prediction of Kraemer and Johnstone (1955), summarised in equation (11):

$$EC_{KJ} = \left(\frac{Q}{\pi\varepsilon_0 A^2 \Delta U}\right)\left(\frac{q \times C_u}{6\pi\eta_{air}a}\right) \tag{11}$$

With η_{air} - the dynamic viscosity of air, C_u - is the Stokes-Cunningham slip correction factor (defined in Appendix A of Dépée et al. (2019)) and ΔU the droplet fall velocity relative to the AP fall velocity. This latter is assumed to be equal to $|U_{A,\infty} - U_{a,\infty}|$ where $U_{a,\infty}$ is the AP settling velocity.

Since this prediction models the contribution of the attractive Coulomb forces on the CE, only the CE measurements with a negative charge product for the 4 AP radii are compared. In Figure 9, the modelled CE from the prediction of Kraemer and Johnstone (1955) as a function of the measured CE is presented. The horizontal error bars are the measurement uncertainties while the vertical ones are the extreme theoretical CE values considering the extreme droplet and AP charges (by adding or subtracting the charge uncertainties). It is shown that the prediction of Kramer and Johnstone (1955) accurately describes the observation for the large charge products (red color) but the discrepancies between model and measurement increase when the charge product decreases. Indeed, the less AP and droplet are electrically charged, the more the model underestimates the CE compared to the observations. This is due to the formula which only models the attractive Coulomb forces and disregards the other effects like the AP weight, the AP inertia and the AP diffusion which tend to increase the CE as well as the diffusiophoretic and the thermophoretic forces (**Dépée et al., 2020**). Consequently, the prediction gives better agreement for large charge products where the attractive Coulomb forces dominate the other effects on the AP collection. This case illustrates the strong interest of using Lagrangian models like the one of Dépée et al. (2019) which considers all microphysical effects involved in the in-cloud AP collection and especially their coupling.
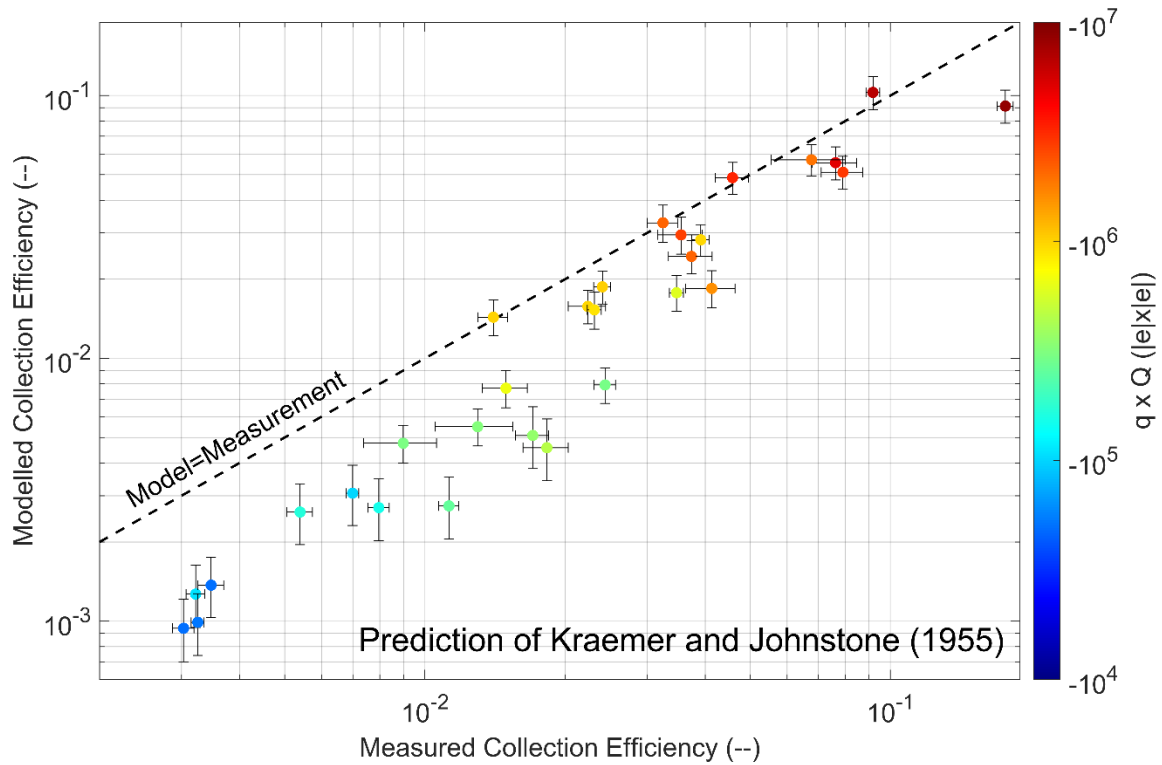
Figure 9 Modelled CE from the prediction of Kraemer and Johnstone (1955) as a function of the measured CE. The droplet radius is 48.5 ± 1.1 µm. Only the negative charge products for the 4 AP radii are considered here, represented by the color code. The experimental conditions are summarised in Table 5.

Note that Wang et al. (1983) also compared their CE measurements with this prediction, finding good agreement since they considered between -10^7 and -10^8 elementary charges on droplets and between 1 and 13.5 elementary charges on APs. So, their charge products were larger than the ones used in the present study and they had no combined effect - the attractive Coulomb force was by far the only significant contribution. It can explain why their comparison with the prediction of Kraemer and Johnstone (1955) are better than the ones presented in Figure 9. Since most of the measurements of Wang et al. (1983) are for a droplet radius of 250 µm, they are not comparable to the present ones which are significantly much smaller (A= 48.5 ± 1.1 µm).

3.2.3.2 Dépée et al. (2019) extended model

In Figure 10, the modelled CE from the extended model of Dépée et al. (2019) as a function of the measured CE is presented. The modelled CE are calculated from the experimental parameters (AP density, air temperature, pressure and relative humidity as well as the sizes and charges) and the CE values less than 10^{-5} are set to 10^{-5} to avoid an excessive computation time (Dépée et al., 2019). The horizontal error bars are the measurement uncertainties while the vertical ones are the extreme theoretical CE values considering the extreme droplet and AP charges (by adding or subtracting the charge uncertainties). The color code corresponds to the different droplet radii studied.

A good accordance between the model and the CE measurements are shown. Indeed, it appears that there are as many data points above the "Model=Measurement" line as below, meaning that the model overestimates as much as underestimates the observations. Thus, it can be assumed that there is no missing or unnecessary microphysics effects in the CE modelling. Moreover, the mean difference between the modelled CEs and the 70 measured CEs is 66 %. This is a reasonable value for a microphysics parameter such as the collection efficiency which varies on several orders of magnitude, especially since the value was calculated disregarding the different uncertainties (error bars in Figure 10) and was as a result over-evaluated.

Nevertheless, 6 data points seem inconsistent with discrepancies between model and measurements from 150 to 1000 %, occurring for the smallest CE values in Figure 10 (lower left). Note that the discrepancies should be even worse since the modelled CEs, set to 10^{-5}, are actually much lower. By examining these data points, it appears that the measured AP masses in the droplet impaction cup - $m_{AP,d}$ in equation (1) - are very close to the detection limit of the spectrometer used. Moreover, for

558   the experimental conditions, the model predicts AP masses in the droplets lower than the detection
559   limit since the Coulomb inverse square term in equation (10) was very repulsive. So, the assumption
560   can be made that a pollution occurred during the various steps of the protocol (end of experiment,
561   disassembly of the chamber's bottom to reach the droplet impaction cup, change of room for the
562   analysis, etc.). Note that the detection limit of the spectrometer is 10^{-15} kg (for the nominal analysis
563   volume considered), which only represents ten APs with a dry radius of 250 nm deposited on the
564   droplet impaction cup. Thus, it exists an important uncertainty in these CE measurements related to
565   a possible contamination. This is difficult to quantify but the low uncertainties of the CE
566   measurements below 10^{-4} were increased in Figure 10. To reduce this potential pollution, it would
567   be necessary to work in a cleanroom or increase the experiment duration to avoid detection problem.
568   However, for these data points the experiment duration was almost 6 hours and, beyond this
569   duration, stability problems of the piezoelectric droplet generator were frequent.
570
571   However, a reasonable agreement between the extended model of Dépée et al. (2019) and the CE
572   measurements are observed. As a reminder, the mean discrepancy was over-evaluated at 66 % which
573   is suitable to describe a microphysical parameter varying on several orders of magnitude for the
574   collection efficiency. Furthermore, if the 6 inconsistent values are removed - the mean discrepancy
575   on the 63 remaining CE measurements decreases from 66 to 38 %.
576
577   The 38 % of discrepancy between the Dépée et al. (2019) extended model and the measurements can
578   be attributed to the dispersion of the AP charge distribution. Indeed, it was not possible to
579   characterize the AP charge distribution which remains an important uncertainty. Moreover, the AP
580   size distribution was assumed to be monodispersed but a dispersion exists, even if very small, which
581   depends on the spectral bandwidth of the DMA. This one can induce some larger (or smaller) APs
582   inside the AP charger which can get an electric charge significantly larger (or smaller) than the
583   predicted one since the charging process is roughly proportional to the AP surface. Then, in the In-
584   CASE chamber, some larger (or smaller) APs with a larger (or smaller) electric charge can interact
585   with the droplets and notably change the final AP mass collected by the droplets during an
586   experiment ($m_{AP,d}$). Another possible explanation is the differences in temperature and relative
587   humidity between the top and the bottom chamber, respectively less than 1°C and 4 % (addressed in
588   **Dépée et al. (2020)**). It could induce local discrepancies during the AP travel time in the chamber in
589   terms of AP density and radius (through the hygroscopicity) or thermophoretic and diffusiophoretic
590   forces which can change the likelihood of being collected by the droplets and then slightly change
591    $m_{AP,d}$. See **Dépée et al. (2020)** for a discussion of the influence of these two latter forces on the CE.
592
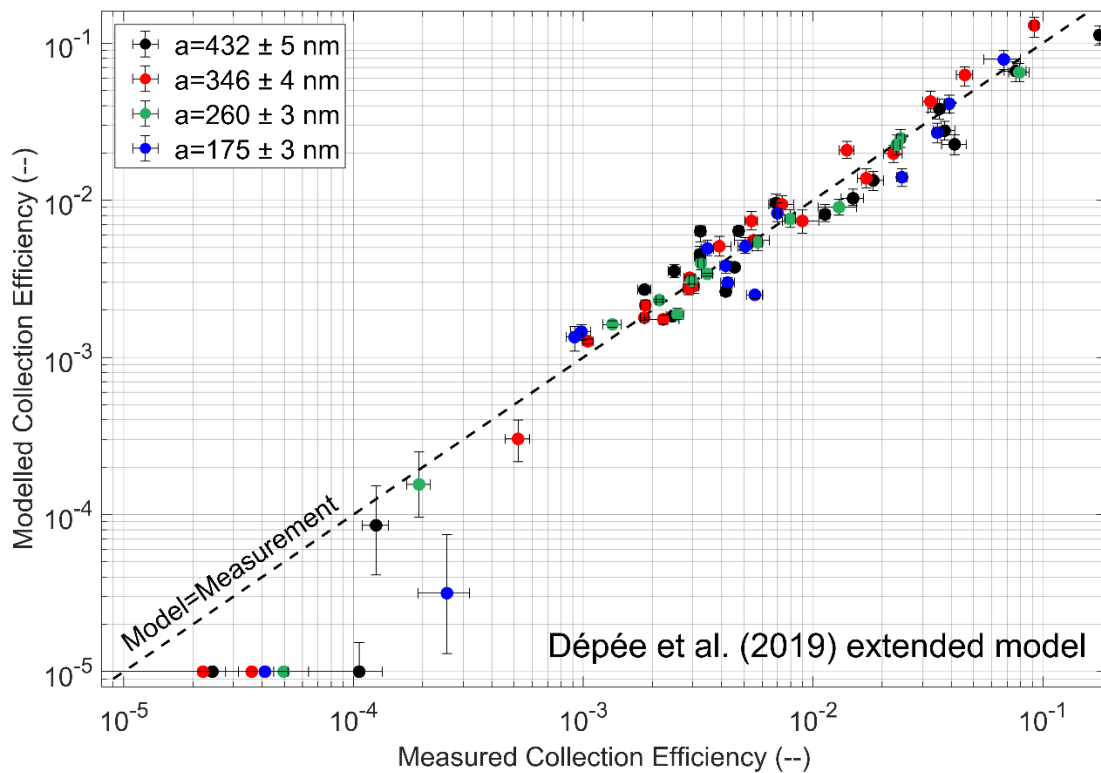
CONCLUSION

599 In-CASE (In-Cloud Aerosol Scavenging Experiment) was developed to conduct a series of experiments
600 evaluating the contribution of microphysical effects on the AP collection by falling cloud droplets.
601 For this purpose, all the parameters influencing the collection efficiency (CE) are controlled - i.e.
602 the AP and droplet sizes, the AP and droplet electric charges and the relative humidity. A first
603 campaign was performed to study the influence of the relative humidity which is the topic of the
604 Part I (**Dépée et al., 2020**). This current study was dedicated to a second topic - aiming the impact
605 of the electric charge on the CE. Furthermore, the CE measurements allow to validate existing models
606 like the Lagrangian one of Dépée et al. (2019) which considers all microphysical effects involved in
607 the AP collection by cloud droplets. Indeed, the literature lacks baseline data to get a suitable
608 comparison with the modelling since most of the previous studies failed to control all parameters
609 influencing the CE like the AP and droplet sizes and charges as well as the relative humidity (Beard,
610 1974; Lai et al., 1978; Barlow and Latham, 1983; Byrne and Jennings, 1993). Even though some studies
611 stand out (Wang and Pruppacher, 1977; Wang et al., 1983), no one examined the influence of the
612 electrostatic forces when the droplet and AP charges had like signs. Thus, the short-range attractive
613 term from the analytical expression of the electrostatic forces - equation (10) - used in the current
614 Lagrangian models (Tinsley and Zhou, 2015; Dépée et al., 2019) has never been experimentally
615 validated or at least emphasised.
616 In the new measured CE dataset, the APs and droplets are accurately charged through custom-made
617 droplet and AP chargers detailed above. Since both charge polarities are found in clouds (Takahashi,
618 1973), the droplets were negatively as well as positively charged during experiments. Moreover,
619 several amounts of elementary charges on the droplet were considered to represent a neutral droplet
620 but also the weakly and strongly charged droplets respectively found in stratiform and convective
621 clouds (Takahashi, 1973). The AP charge varied from zero to -90 ± 9 elementary charges depending
622 on the AP size to represent different amounts of elementary charges encountered in the atmosphere,
623 particularly the ones of radioactive APs. The relative humidity was maximised in this experimental
624 work (**95.1** ± 0.2 %) with a mean temperature in the collision chamber (1.08 ± 0.12 °**C**) stable and
625 comparable with the other study in the companion paper: Part I (**Dépée et al., 2020**). Thus, the

19

thermophoretic and diffusiophoretic contributions on the CE measurements were reduced as much as possible. Nevertheless, since Dépée et al. (2020) measured a significant contribution for a comparable relative humidity level, these two forces were still added to the Dépée et al. (2019) model for a reliable model/measurement comparison. Finally, the droplet radius was 48.5 ± 1.1 µm and 4 wet AP radii were used - from 175 ± 3 to 432 ± 5 nm. Note that the hygroscopicity of the sodium fluorescein salt was considered in the calculation of the wet AP radius and the AP density.

From the 70 measurements obtained, an influence of the electric charges of 4 orders of magnitude on the CE was observed, strongly increasing or decreasing the CE for large charge products, respectively negative or positive. An increase of the CE was also measured by considering more elementary charges on the APs even though the droplets were neutral (within uncertainties). This observation is an important result since it emphasises the contribution of the short-range attractive term in the electrostatic forces (equation (10)). It validates a surface charge distribution on the droplet, formed by the partial influence of the AP electric field on it, which has never been experimentally shown, to our knowledge, in the literature before.

The CE measurements with opposite signs on the droplet and AP were compared to the prediction of Kraemer and Johnstone (1955), giving good agreements for large negative charge products where the Coulomb attractive forces prevail over the other dynamic effects. This is in line with the work of Wang et al. (1983) who also obtained good agreements, considering another droplet radius (250 µm) and larger negative charge products. However, in the present study, an increase of the discrepancies between the prediction and the measurement was measured when reducing the number of elementary charges. This is due to the electrostatic forces not being the only effect involved in the AP collection. There is actually a coupling of electrostatic, diffusiophoretic and thermophoretic forces as well as the AP diffusion, weight and inertia. Thus, when the charge product is not strong enough (gets significantly smaller than 10^7 $|e|x|e|$), Lagrangian models as the one of Dépée et al. (2019) remain the best estimation of the CE.

Finally, the CE measurements were also compared to the extended model of Dépée et al. (2019), showing a really good description of the observed effects. Indeed, the mean discrepancy of the modelling and the 70 measurements was 66 % which is suitable for a microphysical effect varying on several orders of magnitude like the collection efficiency. This value was even better when 6 inconsistent measurements, probably contaminated, were disregarded – as it decreases from 66 % to 38 %. Moreover, note that the model overestimates as much as underestimates the observations so that the discrepancies probably result from remaining uncertainties (like the dispersion of the AP charge distribution) instead of a missing microphysical effect in the CE modelling.

To conclude, 70 new CE measurements are now available that include the influence of the electric charges, showing significant differences with the previous CE measurements and theoretical values from the literature which disregard the electrostatic forces. Thus, it appears to be essential to study the impact of the new baseline data in a cloud-model like DESCAM (Detailed SCAvenging Model, Flossmann, 1985) to examine the influence of the electric charges on the total wet AP removal in the atmosphere. It could strongly affect the atmospheric AP removal since cloud droplets are known to be charged (Takahashi, 1973) as well as the atmospheric AP, even more when APs are radioactive. Indeed, Dépée et al. (2019) estimated that the electric charge of the radioactive APs emitted after the Fukushima accident in 2011 was up to 600 elementary charges. Thus, AP removal could be substantially affected by the electrostatic forces in-cloud and significantly change the ground contamination after a discharge of radioactive materials from a nuclear accident. Since the new Lagrangian model of Dépée et al. (2019) showed an accurate description of the influence of the electric charges (and also of the relative humidity, studied in Part I **(Dépée et al. (2020)**)) on the CE, this latter constitutes a simple, convenient and rapid manner to obtain a CE evaluation for its incorporation in cloud models.

Appendix A - AP charger

A.1 AP charging relationship's acquisition

The AP charging relationships were obtained by performing *ex situ* experiments with the setup presented in Figure A.1. A nominal AP flow goes through the charger with a monodispersed AP size distribution. At the charger's outlet, the flow of charged AP is subdivided - 0.6 l/min is directed to a Condensation Particle Counter (CPC; TSI 3787) to deduce the concentration number of AP in the charger ($C_{N,AP}$) while the other part goes toward an electrometer (TSI 3068A) to measure the current (I_{elect}) due to the charge evacuation. Before entering the CPC, APs are neutralised to avoid any deposition on the metallic walls of the CPC and then the AP flow passes through a diffusion battery to filter the fine particles produced during the discharges inside the charger. The mean AP charge ($\langle q \rangle$) was then calculated from the equation (A.1) with the elementary charge (e) and the AP flowrate in the electrometer (Q_{elect}):

$$\langle q \rangle = \frac{I_{elect}}{e \times C_{N,AP} \times Q_{elect}}$$

(A.1)

Several AP flowrates in the charger ($Q_{charger}$) were considered to study the AP penetration. When $Q_{charger}$ was less than 0.7 l/min, clean air was added before the CPC to maintain a CPC flowrate of 0.6 l/min - this part is presented in red in Figure A.1. From these experiments, it was found that $Q_{charger}$=1.5 l/min maximises the AP penetration through the charger. Note that the AP penetration is defined, at the charger's outlet, as the AP number concentration when the charger is switched on over the AP number concentration when this latter is switched off.
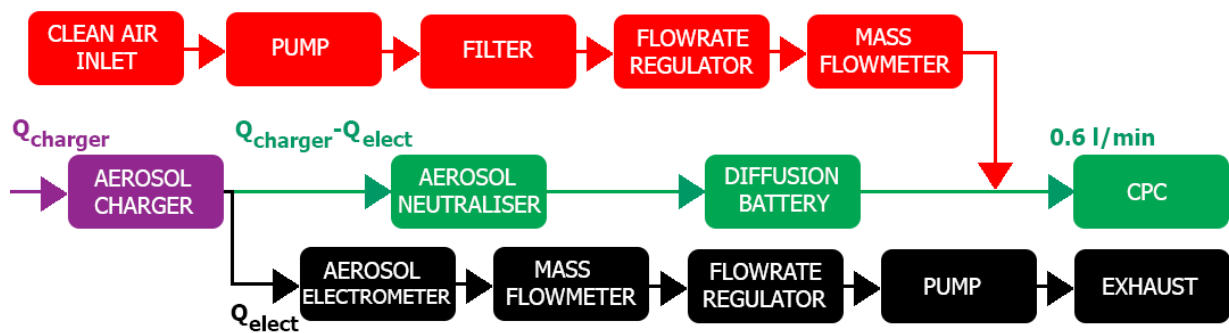
Figure A.1 Setup to obtain the AP charging relationship. The red dashed rectangle is the part added to study the AP penetration through the charger.

A.2 Validation

The setup (Figure A.1) was conducted with the charger turned off to measure the mean AP charge after the DMA. It was found one elementary charge on APs which validates that the multiple charged APs are stopped at the DMA's inlet by the aerodynamic impactor. Thus, the assumption made that the AP size distribution is monodispersed after the DMA is justified. The AP charge was also analysed during 5 hours - no AP charge modification was measured over time. Moreover, the saturated AP charges visible in Figure 4 for a tungsten wire potential less than -12.5 kV was also compared to the theoretical values of Pauthenier and Moreau-Hanot (1932) - giving a good agreement.

Note that two other characterizations were made during these *ex situ* experiments like the determination of the ion current between the grounded cylinder and the tungsten wire (Figure 3) or the discharge frequencies - these both parameters are related to the tungsten wire potential. These curves were used to precisely identify the discharge regime of the charger (Unger, 2001) - the negative Trichel regime which provides a large discharge frequency and then a spatially homogeneous particle charging around the tungsten wires.

Appendix B - Droplet charging relationship obtention

B.1   Overview

Figure B.1 presents the setup used in *ex situ* experiments to measure the droplet charge where the charging relationship in Figure 6 comes from. The housing made with a 3D printer - containing the droplet injector and the charging system (detailed in section 1.5) - is set above a capacitor composed of one neutral potential plate and another plate connected to a high potential (V_{cap}). In this latter, pictures are obtained by optical shadowgraphy to get the droplet trajectories. The electric field (E_{cap}) induced in the capacitor disturbs the droplet motion according to its electric charge. Thus, the droplet charge is evaluated by finding the one which fits the best the theoretical droplet trajectory - deduced from the 2nd Newton's law - and the measured droplet trajectories. A Faraday cage ensures the electric field at the capacitor (E_{cap}) has no effect on the electric field at the electrostatic inductor (E_{ind}). Since this is not a proper Faraday cage because of the holes for droplets and camera, a horizontal metallic perforated plate is added below the droplet generator housing and connected to the neutral potential to prevent the electric field (E_{cap}) from changing the droplet charge.

Figure B.1 Setup to obtain the droplet charging relationship - (**Left** and **Center**) 3D view and (**Right**) schema (not at scale)

B.2   Droplet charge evaluation

A series of 200 pictures pairs, with each one dephased from the other by a known time-step (Δt), are obtained by optical shadowgraphy at the level of the capacitor. A circle Hough transform is then applied to evaluate the droplet centers in every picture - an example is given in Figure B.2 (Left) where the two droplets from a picture are represented by two black crosses meanwhile the blue cross is the detected droplet from the coupled picture dephased by Δt.

Then, the instantaneous droplet velocity $\overrightarrow{U_{D_0}(t)} = U_{D_0,x} \overrightarrow{u_x} + U_{\infty,A} \overrightarrow{u_y}$ at the first detected droplet position (D_0) of coordinates (x_{D_0}, y_{D_0}) is calculated and the vertical velocity component ($U_{\infty,A}$) determines the droplet radius (A) by reversing the Beard (1976) model. Here, the circle Hough transform is not used to calculate the droplet radius like during CE experiments - see Figure 8, right from part I, Dépée et al. (2020). Indeed, the camera zoom is at the lowest to get a large field - the uncertainty would be too large.

Finally, the theoretical droplet trajectories at the capacitor are deduced by solving the 2nd Newton's law where the buoyancy force (F_{buoy}), the drag force (F_{Drag}) and the electrostatic force ($F_{E_{cap}}$) related to the electric field (E_{cap}) at the capacitor are considered, summarised in equations (B.1) :

$$\begin{cases} m_D \dfrac{d\boldsymbol{U}_D(t)}{dt} = \boldsymbol{F}_{buoy} + \boldsymbol{F}_{Drag} + \boldsymbol{F}_{E_{cap}} \\[2mm] \boldsymbol{F}_{buoy} = -m_D \dfrac{\rho_{water} - \rho_{air}}{\rho_{water}} g\, \boldsymbol{u}_y \\[2mm] \boldsymbol{F}_{Drag} = -\dfrac{C_D \pi \rho_{air} U_D{}^2 A^2}{2} \dfrac{\boldsymbol{U}_D(t)}{\|\boldsymbol{U}_D(t)\|} \\[2mm] \boldsymbol{F}_{E_{cap}} = Q E_{cap} \boldsymbol{u}_x \end{cases}$$ (B.1)

754   With $\boldsymbol{U}_D$ - the instantaneous droplet velocity vector at the computational time t, ρ_{air} and ρ_{water} -
755   the air and water densities, g - the acceleration of gravity, m_D - the droplet mass, Q - the droplet
756   charge, C_D - the drag coefficient, $\boldsymbol{u}_x$ and $\boldsymbol{u}_y$ - the unit vectors in the cartesian coordinate system
757   visible in Figure B.2 (Left).
758
759   By projecting on the corresponding axis, it is obtained the system of equations (B.2) to solve:

$$\begin{cases} m_D \dfrac{dU_{D,x}(t)}{dt} = Q E_{cap} - \dfrac{C_{D,x} \pi \rho_{air} U_{D,x}{}^2 A^2}{2} \\[2mm] m_D \dfrac{dU_{D,y}(t)}{dt} = -m_D \dfrac{\rho_{water} - \rho_{air}}{\rho_{water}} g - \dfrac{C_{D,y} \pi \rho_{air} U_{D,y}{}^2 A^2}{2} \end{cases}$$ (B.2)

760   Where $C_{D,x}$ and $C_{D,y}$ are the drag coefficient projections depending on the Reynolds number
761   projections Re_x et Re_y in the cartesian coordinate system. Since $Re_x \ll 1$ et $Re_y < 2$ in the study, the
762   drag coefficient projections are calculated from the analytical expression given by Hinds (2012) and
763   summarised in equations (B.3):

$$\begin{cases} C_{D,x} = \dfrac{24}{Re_x} = \dfrac{12\,\eta_{air}}{A U_{D,x} \rho_{air}} \\[2mm] C_{D,y} = \dfrac{24}{Re_y} \underbrace{\left(1 + 0{,}15 Re_y{}^{0{,}687}\right)}_{①} \approx \dfrac{12\,\eta_{air}}{A U_{D,y} \rho_{air}} \underbrace{\left(1 + 0{,}15 \left(\dfrac{2 A U_{\infty,A} \rho_{air}}{\eta_{air}}\right)^{0{,}687}\right)}_{=K_1} \end{cases}$$ (B.3)

764   Note that the term ① in the Equations (B.3) is supposed as constant to simplify the resolution of the
765   equations (B.1) - giving second order differential equations. This assumption is justified since Re_y is
766   close to the unity and then $C_{T,y} = \frac{24}{Re_y}$ remains suitable. The equation system to solve becomes,
767   equations (B.4):

$$\begin{cases} m_D \dfrac{dU_{D,x}(t)}{dt} = Q E_{cap} - \overbrace{6\pi A \eta_{air}}^{K_2} U_{D,x} \\[2mm] m_D \dfrac{dU_{D,y}(t)}{dt} = -m_D \dfrac{\rho_{water} - \rho_{air}}{\rho_{water}} g - \underbrace{6\pi A \eta_{air} K_1}_{K_3} U_{D,y} \end{cases}$$ (B.4)

768   After two consecutive integrations with the initial conditions - $U_{D,x}(t=0) = U_{D_0,x}$, $U_{D,y}(t=0) = U_{\infty,A}$,
769     $(x_D(t=0), y_D(t=0)) = (x_{D_0}, y_{D_0})$, the analytical equations of the horizontal and vertical droplet
770   positions, respectively referred as x_{th} and y_{th}, are given in equations (B.5):
771

$$\begin{cases} x_{th}(t) = \dfrac{Q\,E_{cap}}{K_2} t + \dfrac{m_D}{K_2}\left(U_{D_0,x} - \dfrac{Q\,E_{cap}}{K_2}\right)\left[1 - e^{-\frac{K_2}{m_D}t}\right] + x_{D_0} \\[3mm] y_{th}(t) = -\dfrac{m_D(\rho_{water} - \rho_{air})}{K_3 \rho_{water}} g t + \dfrac{m_D}{K_3}\left(U_{\infty,A} + \dfrac{m_D(\rho_{water} - \rho_{air})}{K_3 \rho_{water}} g\right)\left[1 - e^{-\frac{K_3}{m_D}t}\right] + y_{D_0} \end{cases}$$

(B.5)

772   Where $E_{cap} = -grad(V) = -\dfrac{V_{cap}}{0{,}01}$ V/m.
773
774   As presented in Figure B.2 (Left), for every pair of pictures, the droplet charge (Q) is then evaluated
775   by looking for the theoretical droplet trajectory from the Equations (B.5) which fits the best with the
776   observed droplet positions. In the given example (Figure B.2, Left), the fitted theoretical trajectory
777   - for V_{ind} = -32.25 V, V_{cap} = -629.5 V, A = 49.5 μm and the air temperature T_{air} = 292.55 K - illustrated
778   by the red line is obtained for a droplet charge (Q) of +9.10e+04 |e|. Finally, this method is applied

779 for the 200 picture pairs to get the mean droplet charge value - visible in Figure B.2 (Right). Note
780 that the standard deviation of the 200 Q values gives the error bars in Figure 6.
781

782
783 Figure B.2 (**Left**) Determination of the theoretical droplet trajectory which fits the best with the
784 observed droplet positions - red line - and deduction of the droplet charge (Q). In this example,
785 V_{ind} = -32.25 V, V_{cap} = -629.5 V, A = 49.5 μm and the air temperature T_{air} = 292.55 K. (**Right, Top**)
786 Terminal velocity measurement, (**Right, Middle**) Droplet radius evaluation by reversing the Beard
787 (1976) model and (**Right, Bottom**) droplet charge deduction for a series of 200 pictures pairs. Mean
788 and standard deviations for the corresponding parameters are presented.

789

B.3   Validation
791 The method presented at the previous section is possible as long as the droplet has reached its
792 terminal velocity. As mentioned in **Dépée et al. (2020)** and visible in Figure 8 (Left) of the same
793 paper, droplets are generated at a velocity larger than their terminal velocity. It has been found that
794 a distance between the droplet generator and the capacitor of 15 cm was large enough to allow
795 droplets to reach their terminal velocity. In the setup in Figure B.1, this requirement prevails.
796
797 An experiment was performed to ensure that reversing the Beard (1976) model was a suitable method
798 to evaluated the droplet radius. For this purpose, the same droplet train was recorded in optical
799 shadowgraphy with a camera zoom at the lowest and at the greatest to respectively apply the Beard
800 (1976) model inversion and the circle Hough transform. In all tests, it was found a discrepancy of less
801 than 2 % between the two methods, giving overvaluations as well as undervaluations when comparing
802 one to the other.
803
804 Also, the disturbance of the electric field at the capacitor (E_{cap}) on the vertical droplet velocity was
804 studied. E_{cap} was then turned on and off to investigate the change in vertical droplet velocity. It was
805 found that during tests, E_{cap} reduced the vertical velocity up to 1.3 %. This situation was for a droplet
806 charge (Q) and a capacitor potential (V_{cap}) both negative. Some other tests also showed that the
807 droplet vertical velocity was increased up to 0.3 %, for a droplet charge and a capacitor potential of
808 unlike sign. Since these two extreme cases respectively represent an undervaluation of less than
809 0.7 % and an overestimation of less than 0.2 % of the droplet radius - this effect was neglected.
810
811 Finally, two other validations can be formulated by examining Figure 6. First, several capacitor
811 potentials (V_{cap}) were used in the tests - from -629.5 to -477.4 V - giving the same charging
812 relationship. The Faraday Cage is consequently reliable, there is not impact of the electric field
813 (E_{cap}) on the droplet charge. Secondly, in the four tests the droplet radius varies from 47.0 to
814 51.2 μm. Thus, the droplet charging system is independent of the droplet size and droplet
815 evaporation.

References

Ardon-Dryer, K., Huang, Y. W., & Cziczo, D. J. (2015). Laboratory studies of collection efficiency of sub-micrometer aerosol particles by cloud droplets on a single-droplet basis.

Barlow, A. K., & Latham, J. (1983). A laboratory study of the scavenging of sub-micron aerosol by charged raindrops. Quarterly Journal of the Royal Meteorological Society, 109(462), 763-770.

Beard, K. V. (1974). Experimental and numerical collision efficiencies for submicron particles scavenged by small raindrops. Journal of the Atmospheric Sciences, 31(6), 1595-1603.

Beard, K. V. (1976). Terminal velocity and shape of cloud and precipitation drops aloft. Journal of the Atmospheric Sciences, 33(5), 851-864.

Byrne, M. A., & Jennings, S. G. (1993). Scavenging of sub-micrometre aerosol particles by water drops. Atmospheric Environment. Part A. General Topics, 27(14), 2099-2105.

Cherrier, G., Belut, E., Gerardin, F., Tanière, A., & Rimbert, N. Aerosol particles scavenging by a droplet: Microphysical modeling in the Greenfield gap. Atmospheric environment, 166, 519-530, 2017.

Chate, D. M., & Pranesha, T. S. Field studies of scavenging of aerosols by rain events. Journal of Aerosol Science, 35(6), 695-706, 2004.

Clement, C. F., & Harrison, R. G. (1992). The charging of radioactive aerosols. Journal of aerosol science, 23(5), 481-504.

Davenport, H. M., & Peters, L. K. Field studies of atmospheric particulate concentration changes during precipitation. Atmospheric Environment (1967), 12(5), 997-1008, 1978.

Dépée, A., Lemaitre, P., Gelain, T., Mathieu, A., Monier, M., & Flossmann, A. (2019). Theoretical study of aerosol particle electroscavenging by clouds. *Journal of Aerosol Science*, *135*, 1-20.

Dépée, A., Lemaitre, P., Gelain, T., Monier, M., & Flossmann, A. (2020). Laboratory study of collection efficiency of submicron aerosol particles by cloud droplets. Part I - Influence of relative humidity. Submitted to Atmospheric Chemistry and Physics, https://acp.copernicus.org/preprints/acp-2020-831/

Dockery, D. W., Schwartz, J., & Spengler, J. D. (1992). Air pollution and daily mortality: associations with particulates and acid aerosols. *Environmental research*, *59*(2), 362-373.

Depuydt, G. Etude expérimentale in situ du potentiel de lessivage de l'aérosol atmosphérique par les précipitations (Doctoral dissertation), 2013.

Flossmann, A. I., Hall, W. D., & Pruppacher, H. R. (1985). A theoretical study of the wet removal of atmospheric pollutants. Part I: The redistribution of aerosol particles captured through nucleation and impaction scavenging by growing cloud drops. *Journal of the Atmospheric Sciences*, *42*(6), 583-606.

Flossmann, A. I. (1998). Interaction of aerosol particles and clouds. *Journal of the atmospheric sciences*, *55*(5), 879-887.

Greenfield, S. M. (1957). Rain scavenging of radioactive particulate matter from the atmosphere. *Journal of Meteorology*, *14*(2), 115-125.

Grover, S. N., & Beard, K. V. (1975). A numerical determination of the efficiency with which electrically charged cloud drops and small raindrops collide with electrically charged spherical particles of various densities. *Journal of the Atmospheric Sciences*, *32*(11), 2156-2165.

Grover, S. N., Pruppacher, H. R., & Hamielec, A. E. (1977). A numerical determination of the efficiency with which spherical aerosol particles collide with spherical water drops due to inertial impaction and phoretic and electrical forces. *Journal of the Atmospheric Sciences*, *34*(10), 1655-1663.

875
876
877 Hinds, W. C. (2012). Aerosol technology: properties, behavior, and measurement of airborne particles.
878 John Wiley & Sons.
879
880 Jackson, J. D. (1999). Classical Electrodynamics.
881
882 Jaenicke, R. (1993). Tropospheric aerosols. In *International Geophysics* (Vol. 54, pp. 1-31). Academic
883 Press.
884
885 Jaworek, A., Adamiak, K., Balachandran, W., Krupa, A., Castle, P., & Machowski, W. (2002). Numerical
886 simulation of scavenging of small particles by charged droplets. Aerosol Science & Technology, 36(9),
887 913-924.
888
889 Kerker, M., & Hampl, V. Scavenging of Aerosol Particles by a Failing Water Drop and Calculation of
890 Washout Coefficients. Journal of the Atmospheric Sciences, 31(5), 1368-1376, 1974.
891
892 Kraemer, H. F., & Johnstone, H. F. (1955). Collection of aerosol particles in presence of electrostatic
893 fields. Industrial & Engineering Chemistry, 47(12), 2426-2434.
894
895 Ladino, L., Stetzer, O., Hattendorf, B., Günther, D., Croft, B., & Lohmann, U. Experimental study of
896 collection efficiencies between submicron aerosols and cloud droplets. Journal of the Atmospheric
897 Sciences, 68(9), 1853-1864, 2011.
898
899 Laguionie, P., Roupsard, P., Maro, D., Solier, L., Rozet, M., Hébert, D., & Connan, O. (2014).
900 Simultaneous quantification of the contributions of dry, washout and rainout deposition to the total
901 deposition of particle-bound 7Be and 210Pb on an urban catchment area on a monthly scale. *Journal
902 of Aerosol Science*, *77*, 67-84.
903
904 Lai, K. Y., Dayan, N., & Kerker, M. (1978). Scavenging of aerosol particles by a falling water drop.
905 Journal of the Atmospheric Sciences, 35(4), 674-682.
906
907 Laakso, L., Grönholm, T., Rannik, Ü., Kosmale, M., Fiedler, V., Vehkamäki, H., & Kulmala, M. Ultrafine
908 particle scavenging coefficients calculated from 6 years field measurements. Atmospheric Environment,
909 37(25), 3605-3613, 2003.
910
911 Lemaitre, P., Querel, A., Monier, M., Menard, T., Porcheron, E., & Flossmann, A. I. Experimental
912 evidence of the rear capture of aerosol particles by raindrops. Atmospheric Chemistry & Physics, 17(6),
913 2017.
914
915 Lemaitre, P., Sow, M., Quérel, A., Dépée, A., Monier, M., Menard, T., & Flossmann, A. (2020).
916 Contribution of Phoretic and Electrostatic Effects to the Collection Efficiency of Submicron Aerosol
917 Particles by Raindrops. *Atmosphere*, *11*(10), 1028.
918
919 Lira, I. (2003). Evaluating the measurement uncertainty: fundamentals and practical guidance.
920
921 Pauthenier, M., & Moreau-Hanot, M. (1932). La charge des particules sphériques dans un champ
922 ionisé.
923
924 Pranesha, T. S., & Kamra, A. K. Scavenging of aerosol particles by large water drops: 1. Neutral case.
925 Journal of Geophysical Research: Atmospheres, 101(D18), 23373-23380, 1996.
926
927 Pruppacher, H. R., & Klett, J. D. (1997). Microphysics of Clouds and Precipitation.
928 (Dordrecht/Boston/London).
929
930 Quérel, A., Lemaitre, P., Monier, M., Porcheron, E., Flossmann, A. I., & Hervo, M. An experiment to
931 measure raindrop collection efficiencies: influence of rear capture. Atmospheric Measurement
932 Techniques, 7(5), 1321-1330, 2014.
933

Reischl, G. P. W. W., John, W., & Devor, W. (1977). Uniform electrical charging of monodisperse aerosols. *Journal of Aerosol Science*, *8*(1), 55-65.

Santachiara, G., Prodi, F., & Belosi, F. (2012). A review of termo-and diffusio-phoresis in the atmospheric aerosol scavenging process. Part 1: Drop scavenging.

Slinn, W. G. N., & Hales, J. M. A reevaluation of the role of thermophoresis as a mechanism of in-and below-cloud scavenging. Journal of the Atmospheric Sciences, 28(8), 1465-1471, 1971.

Slinn, W. G. Precipitation scavenging: some problems, approximate solutions and suggestions for future research (No. BNWL-SA-5062). Battelle Pacific Northwest Labs., Richland, Wash, USA, 1974.

Slinn, W. G. N. Some approximations for the wet and dry removal of particles and gases from the atmosphere. Water, Air, and Soil Pollution, 7(4), 513-543, 1977.

Twomey, S. (1974). Pollution and the planetary albedo. *Atmospheric Environment (1967)*, *8*(12), 1251-1256.

Takahashi, T. (1973). Measurement of electric charge of cloud droplets, drizzle, and raindrops. *Reviews of Geophysics*, *11*(4), 903-924.

Tinsley, B. A., Rohrbaugh, R. P., Hei, M., & Beard, K. V. (2000). Effects of image charges on the scavenging of aerosol particles by cloud droplets and on droplet charging and possible ice nucleation processes. Journal of the atmospheric sciences, 57(13), 2118-2134.

Tinsley, B. A., Zhou, L., & Plemmons, A. (2006). Changes in scavenging of particles by droplets due to weak electrification in clouds. Atmospheric Research, 79(3), 266-295.

Tinsley, B. A., & Zhou, L. (2015). Parameterization of aerosol scavenging due to atmospheric ionization. *Journal of Geophysical Research: Atmospheres*, *120*(16), 8389-8410.

Unger, L. (2001). *Charge d'aérosol par décharge électrique pour la filtration d'effluents particulaires* (Doctoral dissertation, Paris 11).

Unger, L., Boulaud, D., & Borra, J. P. (2004). Unipolar field charging of particles by electrical discharge: effect of particle shape. *Journal of Aerosol Science*, *35*(8), 965-979.

Vohl, O., Mitra, S. K., Wurzler, S., Diehl, K., & Pruppacher, H. R. Collision efficiencies empirically determined from laboratory investigations of collisional growth of small raindrops in a laminar flow field. Atmospheric research, 85(1), 120-125, 2007.

Volken, M., & Schumann, T. A critical review of below-cloud aerosol scavenging results on Mt. Rigi. Water, Air, and Soil Pollution, 68(1-2), 15-28, 1993.

Wang, P. K., & Pruppacher, H. R. (1977). An experimental determination of the efficiency with which aerosol particles are collected by water drops in subsaturated air. Journal of the Atmospheric Sciences, 34(10), 1664-1669.

Wang, P. K., Grover, S. N., & Pruppacher, H. R. (1978). On the effect of electric charges on the scavenging of aerosol particles by clouds and small raindrops. *Journal of the Atmospheric Sciences*, *35*(9), 1735-1743.

Wang, H. C., Leong, K. H., Stukel, J. J., & Hopke, P. K. (1983). Collection of hydrophilic and hydrophobic charged submicron particles by charged water droplets. Journal of aerosol science, 14(6), 703-712.

Young, K. C. The role of contact nucleation in ice phase initiation in clouds. Journal of the Atmospheric Sciences, 31(3), 768-776, 1974.